**Title:** A Novel Pan-RAS Inhibitor with a Unique Mechanism of Action Blocks Tumor Growth in Mouse Models of GI Cancer

**Authors:** [1]*Jeremy B. Foote*[*], [2]*Tyler E. Mattox*[*], [3,12]*Adam B. Keeton*[*],[3,12] *Xi Chen*, [3]*Forrest T. Smith*, [3]*Kristy L. Berry*, [3]*Thomas Holmes*, [3]*Junwei Wang*, [3]*Chung-Hui Huang*, [2]*Antonio B. Ward*, [1]*Cherlene Hardy*, [4]*Karrianne G. Fleten*; [4]*Kjersti Flatmark*; [5]*Karina J. Yoon*, [6]*Sujith Sarvesh*, [6]*Puranchandra Nagaraju Ganji*, [3]*Yulia Maxuitenko*, [3]*Jacob Valiyaveettil*, [6]*Julienne L. Carstens*, [7]*Donald J. Buchsbaum*, [8]*Jennifer Yang*, [9]*Gang Zhou*, [10]*Elmar Nurmemmedov*,[10]*Ivan Babic*,[11]*Vadim Gaponenko*, [11]*Hazem Abdelkarim*, [3]*Amit K. Mitra*, [12]*Michael R. Boyd*, [13]*Upender Manne*, [14]*Sejong Bae*, [6]*Bassel F. El-Rayes*, [3,12]*Gary A. Piazza*

**Affiliations:** [1]Department of Microbiology, University of Alabama at Birmingham, Birmingham AL, [2]University of South Alabama, Mobile, AL; [3]Department of Drug Discovery and Development, Harrison College of Pharmacy, Auburn University, Auburn, AL;[4] Department of Gastroenterological Surgery, Oslo University Hospital, The Radium Hospital, Oslo, Norway and Institute of Clinical Medicine, Faculty of Medicine, University of Oslo, Oslo, Norway; [5]Department of Pharmacology and Toxicology, University of Alabama at Birmingham, Birmingham AL; [6]Department of Hematology and Oncology, University of Alabama at Birmingham, Birmingham, AL; [7]Department of Obstetrics and Gynecology, University of Alabama at Birmingham, Birmingham, AL; [8]University of Connecticut, Mansfield, CT; [9]Georgia Cancer Center, University of Augusta, Augusta, GA: [10]*Celaris Bio LLC, San Diego, CA;* [11]Department of Biochemistry and Molecular Genetics, University of Illinois, Chicago, IL*;* [12]*ADT Pharmaceuticals LLC Orange Beach, AL*.[13]Department of Pathology, University of Alabama at Birmingham, Birmingham, AL. [14]Division of Preventive Medicine, University of Alabama at Birmingham, Birmingham, AL.

* Authors contributed equally to this work.

**Running Title:** *A Novel Pan-RAS Inhibitor for KRAS Mutated GI Cancers*

**Key Words:** KRAS, Pan-RAS inhibitor, Pancreatic Ductal Adenocarcinoma, Colorectal Adenocarcinoma, T cells

Funding Sources: NIH/NCI R01CA254197, R01CA238514, P30CA01314, Richard A. Elkus, M.D., Pilot Grant Program in Pancreatic Cancer Research, and Norwegian Cancer Society 197837.

Corresponding Author: Gary A. Piazza, *W.W. Walker Endowed Professor, Department Head, Drug Discovery and Development, Director, Cancer Research Center, Harrison College of Pharmacy, Auburn University, Auburn, AL,* Walker Building, 362 W. Thach Ave, Room 3306F, Phone: 334-844-7409, gap0034@auburn.edu

**Disclosure of Potential Conflicts of Interest:**

G.A. Piazza, A.B. Keeton, and X. Chen are co-founders of ADT Pharmaceuticals Inc. and consultants. No other authors have conflicts of interest relating to the subject matter.

**ABSTRACT**

Here we characterize a novel pan-RAS inhibitor, ADT-007, that potently and selectively inhibited the growth of histologically diverse cancer cell lines with mutant or activated RAS irrespective of the RAS mutation or isozyme. Growth inhibition was dependent on activated RAS and associated with reduced GTP-RAS levels and MAPK/AKT signaling. ADT-007 bound RAS in lysates from sensitive cells with sub-nanomolar $EC_{50}$ values but did not bind RAS in lysates from insensitive cells with low activated RAS. Insensitivity to ADT-007 was attributed to metabolic deactivation by UGT-mediated glucuronidation, providing a detoxification mechanism to protect normal cells from pan-RAS inhibition. Molecular modeling and experiments using recombinant RAS revealed that ADT-007 binds RAS in a nucleotide-free conformation to block GTP activation. Local injection of ADT-007 strongly inhibited tumor growth in syngeneic immune competent and xenogeneic immune deficient mouse models of colorectal and pancreatic cancer and activated innate and adaptive immunity in the tumor microenvironment.

**SIGNIFICANCE:** ADT-007 is a novel pan-RAS inhibitor with a unique mechanism of action having potential to circumvent resistance to mutant-specific KRAS inhibitors and activate antitumor immunity. The findings support further development of ADT-007 analogs and/or prodrugs with oral bioavailability as a generalizable monotherapy or combined with immunotherapy for RAS mutant cancers.

**BACKGROUND:** It is projected that colorectal cancer (CRC) and pancreatic ductal adenocarcinoma (PDA) will cause 52,580 and 49,830 deaths in the US in 2023, respectively (1). The 5-year survival rates for CRC and PDA are 65% and 12%, respectively (1). Over 50% of CRC and 90% of PDA patients harbor mutations in KRAS genes that are associated with poor prognosis, making the development of novel KRAS inhibitors an urgent unmet medical need (2).

For many cancers, KRAS mutations initiate tumorigenesis that in cooperation with the acquisition of mutations in other oncogenes or inactivating mutations in tumor suppressor genes

such as p53 (3), SMAD4 (4), APC (5), or p16 (6), promote the progression from precancerous lesions to malignant disease. RAS signaling is critical for cancer cell proliferation (7), chemo-resistance (8), metastasis (5, 9), as well as the proliferation of normal cells. KRAS mutations also promote immunosuppression within the tumor microenvironment (TME) through a broad array of mechanisms. Suppressive pathways include increased production of acute inflammatory cytokines (IL-6, IL-8) (10), priming of immunosuppressive T-regs (11) and MDSCs (12), downregulation of MHCI (13), increased expression of programmed cell death ligand 1 (PD-L1) (14), and suppression of intra-tumoral interferon (IFN) signaling (15). Cumulatively, KRAS-mediated reprogramming of the TME results in weakened recognition and reduced cytotoxic T and NK cell functions that support tumor progression.

Recent development of mutant-specific KRAS inhibitors directed against tumors harboring KRAS mutations at the G12C and G12D codons have established KRAS as a druggable target (16). Clinical trials evaluating sotorasib (AMG-510) and adagrasib (MRTX-849) selective for the $KRAS^{G12C}$ mutation reveal promising anti-tumor for NSCLC patients with mutant $KRAS^{G12C}$, but a lower response rate in patients with $KRAS^{G12C}$ mutant CRC (17). Preclinical data indicate critical roles for $KRAS^{G12C}$ and $KRAS^{G12D}$ inhibitors in rewiring the immunosuppressive machinery that limit T cell recognition and cytotoxic activity (18). Another critical issue seen in a high percentage of patients treated with $KRAS^{G12C}$ inhibitors is adaptive resistance mechanisms that limit efficacy (19). These resistance pathways can result from compensation by wild-type (WT) RAS isozymes (HRAS and NRAS) or additional mutations in KRAS (20), making the development of pan-RAS inhibitors a more attractive therapeutic strategy to dampen the RAS-related adaptive resistance circuitry and with the potential for broad use as a monotherapy or in combination with immunotherapy.

Here we characterize a novel, reversible, pan-RAS inhibitor, ADT-007, that was discovered from screening a library of approximately 2000 compounds that shared the indene

scaffold of the nonsteroidal anti-inflammatory drug (NSAID), sulindac. The rationale to screen this focused library for RAS inhibitors was based on a previous report that sulindac and its non-cyclooxygenase inhibitory sulfone metabolite displayed a proportionally greater inhibitory effect on carcinogen-induced mammary tumors harboring mutant HRAS compared with $HRAS^{WT}$ (21). In addition, others have reported that sulindac directly binds RAS and inhibits RAS-induced transformation and signaling, albeit with low potency and confounding effects on cyclooxygenase activity (22, 23). Lacking reactive groups, ADT-007 and a series of analogs emerged after extensive chemical optimization that improved potency and selectivity, including the conversion of the carboxylic acid moiety on sulindac to amides previously reported to disrupt COX-1 and COX-2 binding (24) (**Figure 1A**). A series of cellular, biochemical, and biophysical experiments were then conducted to elucidate the mechanism of action. We also assessed *in vitro* and *in vivo* anticancer activity using human and mouse cells and immune activating potential in mouse models of $KRAS^{G12D/V/C/A}$ driven CRC and PDA.

## RESULTS:

### ADT-007 potently and selectively inhibits the growth of cancer cells with mutated or hyper-activated wild-type RAS isozymes

ADT-007 and a series of analogs were discovered from screening a focused library of indenes for differential growth inhibitory activity in full dose-response using HCT-116 CRC cells harboring a $KRAS^{G13D}$ mutation vs. HT-29 CRC cells with $RAS^{WT}$, but mutant $BRAF^{V600E}$. Among the analogs, ADT-007 (**Figure 1A**) displayed the highest potency and selectivity to inhibit the growth of $KRAS^{G13D}$ HCT-116 cells with an $IC_{50}$ of 5 nM, while $RAS^{WT}$ HT-29 cells were ~100 fold less sensitive with an $IC_{50}$ of 493 nM (**Figure 1B**). Consistent with harboring mutant KRAS, HCT-116 cells expressed high levels of activated (GTP-bound) RAS as measured by RAS-RBD pull-down assays that was essentially undetectable in $RAS^{WT}$ HT-29 cells (**Figure 1B, Inset**). Nonetheless, the growth of both cell lines was dependent on MAPK

signaling given equal sensitivity to inhibitors targeting downstream kinases, RAF and MEK in growth assays (not shown), supporting their use to screen for RAS inhibitors.

ADT-007 displayed even greater potency in $KRAS^{G12C}$ MIA PaCa-2 PDA cells, resulting in $IC_{50}$ values as low as 2 nM and a selectivity index approaching 1200-fold relative to $RAS^{WT}$ BxPC-3 PDA cells **(Table 1)**. ADT-007 also potently inhibited the growth of three other mutant KRAS PDA cell lines with G12V or G12D mutations **(Table 1)** that are more prevalent in PDA patients (25). RAS-RBD pull-down assays confirmed high levels of GTP-RAS among the mutant KRAS PDA cell lines, while activated RAS levels in $RAS^{WT}$ BxPC-3 cells were essentially undetectable (**Supplemental Figure 1A-B**).

The requirement of mutant RAS for sensitivity to ADT-007 was determined by transfecting $RAS^{WT}$ HT-29 cells with $HRAS^{G12V}$, resulting in an $IC_{50}$ of 24 nM vs. 549 and 730 nM for parental and vector control cells, respectively (**Figure 1C**). Similar results were obtained by transfecting $RAS^{WT}$ BxPC-3 cells with mutant $KRAS^{G12C}$ (**Supplemental Figure 2A**). In both isogenic models, the transfection with mutant HRAS or KRAS was confirmed by high levels of GTP-RAS as measured by RAS-RBD pull-down assays (**Figure 1C, Inset and Supplemental Figure 2B)**.

Other experiments showed that ADT-007 treatment of MIA PaCa-2 cells comparably suppressed growth in 2D monolayer and 3D spheroid cultures with $IC_{50}$ values of 2.1 and 3.3 nM, respectively, with unusually step dose-response curves that were a characteristic feature of ADT-007 and analogs (**Supplemental Figure 2C-D**). ADT-007 completely inhibited colony formation of PDA cell lines with G12C, G12D, and G12V KRAS mutations, whereas colony formation of $RAS^{WT}$ BxPC-3 cells was not significantly affected by ADT-007 treatment under identical conditions (**Supplemental Figure 2E**). Complete blockage of colony formation by ADT-007 treatment was also observed in HCT116 cells, but not HT29 cells (not shown).

The anticancer activity ADT-007 was further evaluated in growth assays involving a large panel of histologically diverse tumor cell lines with various mutations in K/N/HRAS isozymes or upstream signaling components that activate RAS such as receptor tyrosine kinases (RTK) or GTPase activating proteins (GAPS) (**Table 1**). Cancer cell lines with mutations in K/N/HRAS isozymes or upstream signaling components (e.g., PDGF, EGFR, or NF1) were uniformly sensitive to ADT-007 with growth $IC_{50}$ values in the single digit nM range. In addition to HT-29 CRC and BxPC-3 PDA cancer cell lines, OV90 ovarian cancer and SK-MEL-28 melanoma cell lines with $RAS^{WT}$ mutant $BRAF^{V600}$ were essentially insensitive to ADT-007. Cells derived from normal colon mucosa (NCM460) or lung airway epithelium (NHAEC) were also insensitive to ADT-007 treatment despite rapid proliferation in culture. These findings lead us to conclude that ADT-007 exhibits pan-RAS inhibitory activity against an array of human cancer cell lines harboring mutant RAS or hyper-activated $RAS^{WT}$ signaling pathways with high selectivity relative to cancer cell lines with downstream mutations or cells from normal tissues.

**ADT-007 inhibits activated RAS and downstream MAPK/AKT signaling in human CRC and PDA cell lines**

Next, we examined the effect of ADT-007 on GTP-RAS levels and downstream signaling through the MAPK/AKT pathways in human CRC and PDA cell lines bearing different KRAS mutations. These experiments were initially conducted under conditions of serum starvation to evaluate treatment effects of ADT-007 resulting from mutant KRAS. A concentration-dependent reduction of GTP-RAS as measured by RAS-RBD pull-down assays was evident at concentrations that inhibited growth and which coincided with reduced downstream phosphorylated levels of RAF, MEK, ERK, and AKT in $KRAS^{G13D}$ HCT-116 cells (**Figure 1D)** and $KRAS^{G12C}$ MIA-PaCa-2 cells (not shown). Similar inhibitory activity of ADT-007 on MAPK/AKT signaling was observed in serum starved, EGF-stimulated MIA PaCa-2 cells (**Figure 1E**). The reduction of GTP-RAS levels by ADT-007 was also apparent in MIA PaCa-2

cells grown in serum or serum starved followed by EGF stimulation (**Supplemental Figures 2F-G**). The pan-RAS inhibitory activity of ADT-007 was confirmed in MIA PaCa-2 cells by measuring activated levels of $HRAS^{WT}$ and $NRAS^{WT}$ isozymes in addition to $KRAS^{G12C}$ with RAS-RBD pull-down assays using pan-RAS and RAS isozyme-specific antibodies following EGF stimulation. As expected, EGF did not activate mutant KRAS but strongly activated $HRAS^{WT}$ and $NRAS^{WT}$. Consistent with a pan-RAS inhibitor, ADT-007 reduced GTP-RAS levels from mutant KRAS and $RAS^{WT}$ isozymes, although with different degrees of potency (**Figure 1F**).

**Comparison with mutant specific KRAS inhibitors**

The pan-RAS inhibitory activity of ADT-007 suggest the potential to circumvent vertical pathways of adaptive resistance (19) mediated by compensatory hyperactivation of $RAS^{WT}$ isozymes in KRAS mutant cells that have been demonstrated to limit or override the anticancer activity of a $KRAS^{G12C}$ specific inhibitors (19). To test this hypothesis, the growth inhibitory activity of ADT-007 was compared to $KRAS^{G12C}$ specific inhibitors in MIA PaCa-2 cell lines that developed resistance to AMG-510 or MRTX-1257 as previously reported (26). ADT-007 showed comparable growth $IC_{50}$ values in cells that developed resistance to AMG-510 and MRTX-1257 as the parental cells, while treatment with AMG-510 and MRTX-1257 resulted in significantly higher growth $IC_{50}$ values in the resistant cell lines relative to parental cells (**Figure 1G**). In addition, we noted that ADT-007 exhibited 10x greater potency than AMG-510 in growth assays involving parental mutant $KRAS^{G12C}$ MIA PaCa-2 cells (**Supplemental Figure 2H**) and a greater difference in potency with longer treatment duration in colony formation assays (not shown). In other experiments, we found that Lewis lung cancer (LLC) cells that harbor a $KRAS^{G12C}$ mutation and an additional mutation, $NRAS^{Q61H}$, were completely insensitive to AMG-510 in growth assays (**Figure 1H**), which is consistent with what others have reported (26)**,** whereas ADT-007 potently inhibited growth with an $IC_{50}$ value of 9 nM. Together, these results

show that ADT-007 maintains potency when cells are chronically exposed to $KRAS^{G12C}$ mutant specific inhibitors or in the presence of two independent activating RAS mutations as well as displaying greater intrinsic potency compared with AMG-510. These findings highlight fundamental advantages of a pan-RAS inhibitor over mutant-specific KRAS inhibitors, which are known from clinical trials to have modest efficacy or are prone to resistance with acquisition of additional cis- or trans-mutations in RAS alleles (19, 27).

**ADT-007 blockade of RAS activation and MAPK/AKT signaling and associated cell cycle arrest and apoptosis**

The impact of ADT-007 on cell cycle distribution and apoptosis was determined in KRAS mutant and $RAS^{WT}$ cell lines. ADT-007 induced G2/M cell cycle arrest in mutant RAS HCT-116 and MIA PaCa-2 cells at concentrations as low as 4 nM, while $RAS^{WT}$ HT-29 and BxPC-3 cells displayed profoundly reduced sensitivity (**Supplemental Figure 3A-D**). ADT-007 also increased levels of active, cleaved caspase 3 in MIA PaCa-2 cells but occurred at times following cell cycle arrest (**Supplemental Figure 3E**). ADT-007 also induced apoptosis of mutant KRAS HCT-116 cells but not $RAS^{WT}$ HT-29 cells if treated under identical conditions as measured by annexin V and cleaved caspase (not shown).

Given the effect of ADT-007 on G2/M arrest and previous studies suggesting that certain other sulindac derivatives chemically similar to ADT-007 with a trimethoxyphenyl moiety that resemble colchicine can inhibit tubulin polymerization (28), the activity of ADT-007 on the polymerization of purified α-tubulin was examined. ADT-007 exhibited a weak inhibitory effect on tubulin polymerization at a concentration 100-fold above its growth $IC_{50}$ value, making a direct link between effects on tubulin polymerization and cell cycle arrest unlikely. (**Supplemental Figure 3F**).

**Chemical moieties impacting potency and selectivity of ADT-007**

From an extensive analysis of structure-activity relationships among ADT-007 analogs, we found that the potency to inhibit growth was significantly reduced and RAS selectivity was

completely abolished when the hydroxyl moiety on the phenolic ring was substituted with a methoxy moiety. This is shown by a closely related trimethoxy analog, ADT-106, that displayed reduced potency compared to ADT-007 (150 nM vs. 2 nM) and lacked selectivity for $KRAS^{G12C}$ MIA-PaCa-2 PDA cells vs. $RAS^{WT}$ BxPC-3 PDA cells in growth assays. Coinciding with the lack of selectivity in growth assays, ADT-106 did not impact EGF-stimulated levels of GTP-RAS levels as ADT-007 (**Supplemental Figure 4A-B**).

*Ex vivo* liver microsome experiments revealed that ADT-007 is rapidly metabolized by glucuronidation of the phenolic OH moiety from UDP-glucuronosyltransferases (UGT). This led us to hypothesize that glucuronidation may account for the insensitivity of normal cells to pan-RAS inhibition by ADT-007 by causing metabolic deactivation from UGT isozymes. Measurement of UGT protein expression using a pan-UGT1 antibody revealed high UGT expression in HT-29 and BxPC-3 cells that are insensitive to ADT-007 compared with sensitive HCT-116 and MIA PaCa-2 cells (**Supplemental Figures 4C-D**). Transcriptomic analysis (RNAseq) of these cell lines and other cell lines in Table 1 (Cancer Cell Line Encyclopedia) describing mRNA expression of six distinct UDP-glucuronosyltransferase isoforms (UGT1A1, 1A6, 1A10, 2A1, 2B10, and 2B15) (29) confirmed low expression of UGT mRNA levels in cancer cell lines that were sensitive to ADT-007, while cell lines insensitive to ADT-007 expressed higher UGT mRNA levels (**Table 1 and Supplemental Table 1**). Measurement of ADT-007 levels by LC-MS/MS from cells treated overnight with ADT-007 revealed 350-fold higher intracellular levels in sensitive HCT-116 cells compared with insensitive HT-29 cells (**Supplemental Figures 4E**). Consistent with the hypothesis that UGT deactivates ADT-007 in RAS WT cells, a higher ratio of the glucuronide conjugated form of ADT-007 was measured in $RAS^{WT}$ HT-29 cells, while no glucuronidated ADT-007 was detected in KRAS mutant HCT-116 cells (**Supplemental Figure 4F**). Experiments using a competitive UGT inhibitor, propofol, showed that pretreatment with propofol increased the sensitivity of $RAS^{WT}$ HT-29 and BxPC-3

cells to ADT-007 in growth assays, decreasing the $IC_{50}$ value by 26- and 18-fold, respectively, without significantly affecting the growth $IC_{50}$ values in KRAS mutant HCT-116 and MIA PaCa-2 cells (**Supplemental Figure 4G**). Together, these results suggest that insensitivity of cancer cells with low activated RAS to ADT-007 is attributed to high UGT levels, which may model normal cells that have a unique protective mechanism to ADT-007 by metabolic detoxification from high UGT levels.

**ADT-007 selectively binds RAS in KRAS mutant cells**

The ability of ADT-007 to directly bind KRAS in cell lysates and intact cells was determined using a cellular thermal shift assay (CETSA). Initial experiments measured the optimal temperature to denature 75% ($T_{agg75}$) KRAS in whole cell lysates followed by western blot (WB) quantification of non-denatured KRAS levels. Treating HCT-116 lysates with ADT-007 increased RAS thermal stability ($T_{agg75}$) with an $EC_{50}$ of 0.45 nM, indicating binding to RAS at concentrations 10-fold below growth $IC_{50}$ values. By comparison, ADT-007 did not affect thermal stability of $RAS^{WT}$ in HT-29 cells **(Figure 2A)**. ADT-007 also did not bind an unrelated protein, phosphodiesterase 10A (PDE10) that was used as a negative control (not shown). In other experiments involving ADT-007 treatment of intact HEK293 embryonic kidney cells transfected with epitope tagged mutant $KRAS^{G12C}$, WB analysis with anti-Micro-Tag antibody revealed an $EC_{50}$ value of 6.7 nM for ADT-007 (**Figure 2B**), comparable with growth $IC_{50}$ values in cell lines sensitive to ADT-007. By contrast, a trimethoxy analog of ADT-007 (ADT-652) lacking RAS selectivity in growth assays did not bind KRAS (**Figure 2B**). On the other hand, ADT-652 and other trimethoxy derivatives inhibited PDE10 enzymatic activity (cGMP hydrolysis) as previously reported (30) and bound PDE10 as determined by CETSA from treating either cell lysates or intact cells (not shown). These findings indicate high affinity binding of ADT-007 to RAS in cells that is consistent with its high potency and selectivity to inhibit RAS-driven cancer cell growth, activated RAS levels, and MAPK/AKT signaling.

**ADT-007 preferentially binds nucleotide-free RAS**

Molecular docking studies were conducted to gain insight into the mechanism of ADT-007 binding to RAS using $KRAS^{WT}$ (PDB ID 4OBE) given the ability of ADT-007 to inhibit the growth of mutant RAS or $RAS^{WT}$ cell lines with activated RAS. Docking experiments were performed with GDP removed and with either $Mg^{+2}$ present or removed since it was uncertain as to which conformation of KRAS could be preferred for ADT-007 binding **(Supplemental Figure 5A-B)**. Molecular dynamics and induced fit docking were used to identify potential binding sites on KRAS (31-33). There was a difference in the predicted orientation of ADT-007 within its preferred binding site when $Mg^{+2}$ was present versus when $Mg^{+2}$ was absent **(Supplemental Figure 5C-D)**. When $Mg^{+2}$ was present the phenolic OH group of ADT-007 was predicted to H-bond with S17 through a water bridge and with E31 through a direct H-bond. When $Mg^{+2}$ was absent the phenolic OH was predicted to interact with D119 via a water bridge and A146 by a direct H-bond. In the cases of $Mg^{+2}$ being present and absent, the best GLIDE docking scores (-11.08 and -12.06 respectively) were obtained with ADT-007 binding to a site partially overlapping the nucleotide binding site that was associated with an altered conformation of the switch-1 region **(Supplemental Figure 5A-B)**. In both cases, the GLIDE docking score of GDP (-9.6 and -8.80, respectively) was appreciably less favorable than ADT-007. This suggested that a conformational change induced by the binding of ADT-007 to RAS may decrease the affinity for nucleotide binding, given that the binding score of GDP to RAS without ADT-007 was -15.16. The results led us to conclude that there may be preference for ADT-007 binding to RAS when in an apoenzyme conformation without bound $Mg^{+2}$ essential for nucleotide binding (i.e., nucleotide-free RAS or nf-RAS) and that ADT-007 binds RAS with higher affinity to this site than nucleotide.

To test experimentally the possibility that ADT-007 preferentially binds nf-KRAS, we determined the ability of ADT-007 to inhibit RAS-RAF interactions using either nf-KRAS or

nucleotide-loaded RAS in a cell-free, reconstituted system with recombinant full-length $KRAS^{WT}$ and measured activated RAS by RAS-RBD pull-down assays. nf-RAS was generated by incubating with EDTA to chelate $Mg^{+2}$ to simulate GEF removal of GDP. ADT-007 treatment before GTP addition inhibited nf-KRAS from binding RAF at concentrations comparable to growth $IC_{50}$ values, while there was a negligible effect when ADT-007 was added to KRAS that was preloaded with GTP (**Figure 2C-D**). Consistent with molecular docking studies, these results suggest the apoenzyme state of RAS is the preferred conformation for binding ADT-007.

We also utilized a nucleotide exchange assay to measure the effect of ADT-007 on the kinetics of GTP binding to WT nf-KRAS using a fluorescent GTP analog (Mant-GTP). These experiments revealed that ADT-007 reduced the rate of GTP binding to RAS if pretreated with EDTA to chelate $Mg^{2+}$ (**Figure 2E**), but not in the presence of the non-hydrolysable GTP analog, GTPγS (**Figure 2F**). In addition, a tool compound, CID1067700, previously reported as a pan GTPase inhibitor, inhibited Mant-GTP binding to RAS to a comparable extent as ADT-007 (not shown) (33).

Experiments involving protein nuclear magnetic resonance (NMR) spectroscopy were also conducted to better define the molecular determinants responsible for the biochemical findings. First, we compared $^{15}N$-HSQC spectra using full length (FL) GDP-KRAS-$4B^{WT}$ recombinant protein alone and in the presence of ADT-007 at a 1:5 protein to compound molar ratio. Consistent with biochemical experiments, NMR spectroscopy showed no significant spectral differences under these conditions, suggesting a low likelihood of direct binding of ADT-007 to the inactive form of RAS (**Supplemental Figure 6**). To further investigate the possibility that ADT-007 binds RAS when in a nucleotide-free conformation, $Mg^{2+}$ from KRAS was chelated with EDTA to allow for the dissociation of GDP from KRAS. These conditions resulted in NMR spectral features distinct from GDP-KRAS, including signal shifts from two key amino acid residues, G13, a hotspot mutation site in the P-loop (32), and K16 that is adjacent to S17, which

is critical for $Mg^{2+}$ binding (31), both of which could be readily identified from their unique resonance frequencies (**Supplemental Figure 7**). Subsequent addition of ADT-007 at a 1:5 protein to compound molar ratio led to statistically significant shifts or attenuation of several HN signals including G13 and K16 in the KRAS catalytic domain that interact with nucleotide (**Figure 3**). NMR signal attenuation in the presence of ADT-007 indicates binding to KRAS leading to intermediate exchange between the compound-occupied and $Mg^{2+}$ free KRAS or altered backbone dynamics in the compound binding site. These results support the preferential binding of ADT-007 to nf-RAS with no evidence of binding to the inactive form of RAS.

**ADT-007 inhibits tumor growth and RAS signaling *in vivo***

To determine *in vivo* anticancer activity, we evaluated whether local administration of ADT-007 (5 mg/kg, BID, 14 days) via peri- or intra-tumoral injection (minimizing hepatic glucuronidation) could inhibit growth in an array of subcutaneous and peritoneal PDA and CRC models, as well as PDX lines with different KRAS mutational status. In the $KRAS^{G12V}$ gall bladder adenocarcinoma (GBA) PDX model, ADT-007 completely arrested cell growth and induced partial regression (**Figure 4A** left and right panels) and caused growth arrest in a $KRAS^{G12C}$ PDA PDX model (data not shown). The activity of ADT-007 was then investigated in three peritoneal metastasis PDX models bearing the following mutations: codon G12A mutation (PMCA-1) (**Figure 4B**), G12D mutation (PMP1) (**Figure 4C**) or KRAS WT and *PDGFRA* T922I mutation (PC244) (**Figure 4D**). Representative growth curves (**Figure 4B-D, left panels**) and tumor volumes at the end of treatment (right panels) are displayed for each model system (**Figure 4B-D, right panels**). ADT-007 significantly reduced tumor outgrowth in all three models. Of the three models, PMCA-1 was the most sensitive where the growth inhibitory effect persisted for a substantial duration of time after discontinuation of treatment and two mice were considered cured, or tumor free on day 100. Consistent with experiments involving cell lines as

described in **Table 1**, the PC244 PDX model expressing WT RAS isozymes, but a suspected activating mutation in PDGFR, was equally sensitive to ADT-007 *in vivo*. Furthermore, reductions in mucin production were notable by MRI in a dose dependent fashion (**Supplemental Figure 8A**) with tumor volumes exhibiting a dose dependency in each model (**Supplemental Figure 8B-D**). Overall, these findings indicate that ADT-007 induces growth arrest and in some cases regression of established and metastatic PDX PDA and CRC tumors, respectively, in immune deficient recipient mouse models.

Antitumor activity of ADT-007 against an array of syngeneic, CRC and PDA tumor cell lines bearing $KRAS^{G12D}$ mutations using immune competent mouse models was also evaluated. When administered by intratumor (IT) injection, ADT-007 (10 mg/kg, qd) strongly inhibited SC tumor growth ($T/C_{max}$ of 27%) in the KRAS mutant CT26 colon tumor model (**Figure 4E, left panel**) with an 80% reduction in mean tumor growth compared to sham treated mice (**Figure 4E, right panel**). Among the mice that were treated with ADT-007, we observed a close association between the reduction of tumor growth as measured by tumor volume relative to sham treated mice, and reduced phosphorylated RAF, MEK, and ERK (**Supplemental Figure 9**).

Peritumoral administration of ADT-007 (5 mg/kg, BID, administered for 17-24 days) induced growth arrest in syngeneic mouse PDA models including previously characterized cell lines 2838c3 (**Figure 4F, left panel**) and 7160c2 (**Figure 4G, left panel**) (34), and a novel KPC cell line 5363 (**Figure 4H, left panel**) with variable patterns of growth arrest to regression noted (**Figure 4F-H, right panels**). Overall, these findings indicate that ADT-007 inhibits growth of mouse and human tumor cell lines bearing different KRAS mutations or those exhibiting hyperactivation of WT KRAS, which is consistent with its mechanism of action as a pan-RAS inhibitor.

**ADT-007-mediated inhibition of KRAS$^{G12D}$ alters the tumor immune microenvironment (TiME)**

The above findings indicate that ADT-007 induces growth arrest, tumor regression, or growth delays in human PDX and syngeneic mouse CRC and PDA tumors. Given the increasing literature on the impact of mutation-specific KRAS$^{G12C}$ (18, 35) and KRAS$^{G12D}$ inhibitors (36) on tumor-specific immunity, we assessed the activity of ADT-007 in syngeneic, immune competent mouse models of CRC and PDA bearing KRAS$^{G12D}$ mutation. To evaluate the impact of ADT-007 on the PDA TiME, we choose two genetically characterized cell lines bearing increased T cell infiltrate (2838c3 and 7160c2) but different levels of T cell priming and activation with the 2838c3 model exhibiting increased priming and activation of CD8 T cells (34). At termination of treatment, 2838c3 and 7160c2 tumor bearing mice were euthanized, and tumors collected to evaluate changes in YFP$^{+}$ tumor and CD11b$^{+/-}$ myeloid cell subsets within the TiME. In both models, ADT-007 decreased the proportion of YFP$^{+}$ tumor cells (**Figure 5A and E**) consistent with reductions in tumor weights (not shown) and growth arrest (**Figures 4F-G**).

Using multiparameter flow cytometry (**Supplemental Figure 10**), proportions of myeloid subsets with the 7160c2 and 2838c3 PDA TiME were evaluated. ADT-007 treatment increased proportions of CD11b$^{+}$ Ly6G$^{+}$ Ly6C$^{+}$ gMDSC and CD11b$^{+}$ Ly6G$^{-}$ Ly6C$^{hi}$ mMDSC subsets in 7160c2, but not in ADT-007 treated 2838c3 tumor bearing mice (**Figure 5B***,7160c2* and **5F***,2838c3*). A significant increase in dendritic cell subsets and macrophage frequencies were noted in 7160c2, but not 2838c3 tumor bearing mice (**Figures 5C-D***,7160c2* and **5G-H***,2838c3*). Analysis of CD11b$^{+}$ F4/80$^{+}$ macrophage phenotypes in both models, specifically focusing on M1 (CD86 and MHCII) and M2 (CD206) markers, revealed trends for decreasing MHCII and CD206 expression in both models (**Figure 5D***,7160c2* and **5H**,2838c3) suggesting that local administration of ADT-007 may globally impact macrophage polarization in the PDA TiME.

Given the critical importance of cytotoxic T cell responses in the TiME as they correlate with tumor regression, we evaluated the relative importance of the adaptive immune system in the *in vivo* efficacy of ADT-007 in 2838c3 and 7160c2 PDA models. Each cell line was implanted into immune competent C57BL/6 mice or C57BL/6 Rag $1^{-/-}$ mice lacking T and B cells to determine if the absence of adaptive immunity had an impact on the efficacy of ADT-007 *in vivo*. When tumors reached 150 $mm^3$ mice were treated with peri-tumoral injections of ADT-007 and sham (vehicle) for a period of 17-20 days dependent on tumor growth kinetics and development of ulcerative lesions. Treatment with ADT-007 reduced growth in both immune competent C57BL/6 and immune deficient C57BL/6 Rag $1^{-/-}$ mice, however, the efficacy of ADT-007 was reduced in C57BL/6 Rag $1^{-/-}$ recipient mice with both models (**Figure 6A***,7160c2* and **6E***,2838c3*), suggesting a role for the adaptive immune response in control of SQ tumor growth during ADT-007 administration.

To understand the effect of ADT-007 on the adaptive immune response, we evaluated whether ADT-007 treatment altered proportions, activation status, and function of NK and T cell subsets in the 7160c2 and 2838c3 TiME using multi-parameter flow cytometry (**Supplemental Figure 11**). ADT-007 treatment resulted in reduced proportions of $CD3^+$ $CD4^+$ $Foxp3^+$ (Tregs), and $CD3^+$ $CD8^+$ (CTLs) T cells, and $CD3^+$ $NK1.1^-$ (NK) cells, whereas $CD3^+$ $TCR\gamma\delta^+$ (γδ T) T cells were increased in the 7160c2, but not 2838c3 TME (**Figure 6B***, 7160c2* **and 6H***, 2838c3*). Next, we evaluated the activation status of T cell subsets by expression of CD44 and CD62L to identify the proportions of naïve ($CD62L^+$ $CD44^-$), pre-effector ($CD62L^-$ $CD44^-$), effector memory ($CD62L^-$ $CD44^{hi}$), and central memory ($CD62L^+$ $CD44^{hi}$) T cells within each subset. T cell phenotypes in the 7160c2 TiME shifted to a $CD44^{hi}$ $CD62L^-$effector memory phenotype with ADT-007 treatment (**Figure 6C)**. In comparison, ADT-007 treatment of 2838c3 tumors increased proportions of pre-effector and effector memory phenotypes in the $CD4^+$ $Foxp3^-$ and $CD3^+$ γδ T cell subsets (**Figure 6I** and data not shown). Expression of PD-1 was increased on

CD4 and CD8$^+$ T cells in 7160c2, but not 2838c3 (**Figure 6D**, 7160c2 and **J**, *2838c3*) indicating that ADT-007 induces T cell activation in the 7160c2 model. Evaluation of production of IL-2, IFNγ, TNFα, and granzyme B in T cell subsets were assessed by intracellular staining after PMA and ionomycin stimulation in the presence of brefeldin A. In the 7160c2 TiME both CD4$^+$ and CD8$^+$ T cells exhibited increased production of IL-2, granzyme B, IFNγ, and TNFα (**Figures 6E and F**); whereas minimal changes in cytokine expression were noted in T cells within the 2838c3 TiME (**Figures 6J and K**). Overall, these findings indicate that ADT-007 modulates function of T cells and inflammatory cytokine production in syngeneic, immune competent mouse models of PDA.

To further refine our understanding of ADT-007 on modulation of cytotoxic activity in mouse models of PDA, we assessed *in vivo*, effector activities of NK and T cells using an IFNγ-Thy1.1 reporter model system (37), where induction of IFNγ results in expression of surface Thy1.1 providing the ability to trace history and active IFNγ production through surface expression of Thy1.1. Using this model, we evaluated the impact of ADT-007 on IFNγ production history of NK and T cell subsets in both the 2838c3 and 7160c2 PDA TiMEs. Consistent with intracellular cytokine staining after PMA + ionomycin stimulation, ADT-007 increased IFNγ production in T cell subsets in the 7160c2, but not 2838c3 PDA TiME. In contrast, ADT-007 reduced Th1.1 expression on NK cells compared to sham treatment (**Supplemental Figure 12A**, *7160c2* **and 12B**, *2838c3*) in both models. Interestingly, Thy1.1 expression was significantly reduced in CD4$^+$ Foxp3$^+$ regulatory T cells in 7160c2, but not 2838c3 TiME, indicating a reduction of IFNγ production by regulatory T cells (**Supplemental Figure 12A**). Overall, these findings suggest that ADT-007 modulates immune responses in the PDA TME in a model specific manner that requires further study.

## Discussion

ADT-007 potently and selectively inhibited the growth of histologically diverse human cancer cell lines with mutant or activated RAS regardless of the RAS mutational codon or isozyme. Closely associated with its selective growth inhibitory activity, ADT-007 suppressed activated RAS levels and MAPK/AKT signaling, resulting in mitotic arrest and apoptosis of RAS mutant cancer cell lines. Cancer cell lines with WT RAS but a downstream mutation in BRAF, and cells from normal tissues, were essentially insensitive to ADT-007. The pan-RAS inhibitory activity of ADT-007 was evidenced using RAS isozyme-specific antibodies in RAS-RBD pull-down assays. ADT-007 treatment of mutant KRAS cells reduced activated KRAS and co-expressed $HRAS^{WT}$ and $NRAS^{WT}$ isozymes that were activated in response to EGF stimulation. Results from CETSA, molecular modeling, and cell-free experiments with recombinant RAS involving biochemical methods and NMR, revealed high affinity and preferential binding of ADT-007 to nf-RAS without binding to the inactive (GDP-bound) form of RAS. We attribute the potency and selectivity of ADT-007 to its ability to bind nf-RAS and prevent GTP activation of effector interactions; the rapid cycling of cancer cells with mutant RAS and their addiction to RAS for proliferation; as well as the unique chemical composition of ADT-007, which as discussed below, renders ADT-007 to be a substrate for glucuronidation by UGT isozymes that are expressed in normal cells, as well as cancer cells with $RAS^{WT}$, but not in cancer cells with mutant RAS.

Local injection of ADT-007 to avoid glucuronidation from liver UGT strongly inhibited tumor growth in immunodeficient and syngeneic murine models of CRC and PDA with partial dependence on the adaptive immune system. ADT-007 activated T cells and enhanced their cytotoxic functions in $KRAS^{G12D}$ mutated CRC and PDA, immune competent mouse models. Together, these studies support the development of orally bioavailable analogs or prodrugs of ADT-007 for RAS-driven cancers and further discussed below.

**ADT-007 specificity for RAS binding**

Evidence that ADT-007 preferentially binds nf-RAS was initially obtained by molecular docking using a combination of molecular dynamics and induced fit with a $KRAS^{WT}$ crystal structure. These studies generated the highest docking score for ADT-007 to a site partially overlapping the nucleotide binding site that was associated with an altered conformation of the switch-1 region. Interestingly, the docking score for RAS to bind nucleotide in the conformation induced by ADT-007 (without $Mg^{2+}$) was appreciably less than the docking score for nucleotide in the absence of ADT-007 (-8.80 vs. -15.16).

Biochemical experiments using recombinant $KRAS^{WT}$ provided experimental evidence that ADT-007 inhibited GTP binding to nf-RAS and RAS-RAF effector interactions. NMR spectroscopy confirmed these observations by showing ADT-007 binding to nf-RAS, but not nucleotide-loaded (inactive) RAS. Previous studies have reported that a fraction of RAS exists in cells as a nucleotide-free transitional conformation (38). This supports the likelihood that ADT-007 inhibits RAS-driven cancer cell growth by binding nf-RAS to block GTP binding either directly (e.g., as a competitive inhibitor) or because of a conformational change in RAS induced by ADT-007 binding outside of the catalytic domain, to disrupt RAS-effector interactions.

CETSA provided further evidence for binding ADT-007 to RAS in cells. ADT-007 treatment of lysates from $KRAS^{G13D}$ mutant HCT-116 cells resulted in sub-nanomolar $EC_{50}$ values for binding. In addition, ADT-007 treatment of intact $KRAS^{WT}$ HEK293 cells transfected with a $KRAS^{G12C}$ mutant allele resulted in $EC_{50}$ values for binding within the same range as growth $IC_{50}$ values. Interestingly, we observed no evidence of ADT-007 binding to RAS by treating lysates from $KRAS^{WT}$ HT-29 cells, which may be attributed to low levels of activated RAS and/or metabolic deactivation of ADT-007 by UGT isozymes remaining active in cell lysates. These results, along with experiments showing induction of sensitivity to ADT-007 by transfecting $RAS^{WT}$ cells with mutant HRAS or KRAS alleles, lead us to conclude that activated or mutant RAS is essential for sensitivity to ADT-007.

Metabolic deactivation of ADT-007 by UGT-mediated glucuronidation also appears to be a factor impacting sensitivity, which has implications for our interpretation of both *in vitro* and *in vivo* experiments. Liver microsome experiments showed that ADT-007 is rapidly glucuronidated by UGT, which are well known to metabolize compounds with phenolic OH moieties. Unexpectedly, cancer cells with $RAS^{WT}$ but downstream mutations in BRAF expressed appreciably higher mRNA and protein levels of major UGT isozymes than cancer cells with mutant RAS. The significance of these differences was apparent by measuring cellular levels of ADT-007 by LC/MS-MS following overnight treatment of mutant RAS or $RAS^{WT}$ cells with ADT-007. These experiments revealed high ADT-007 levels and undetectable ADT-007 glucuronide levels in mutant $KRAS^{G13D}$ HCT-116 cells, but low ADT-007 levels and high ADT-007 glucuronide levels in $KRAS^{WT}$ HT-29 cells. Moreover, pretreatment with a known competitive UGT inhibitor, propofol, increased sensitivity to ADT-007 in cells with $RAS^{WT}$, but not in mutant KRAS cells. These results suggest that UGT-mediated glucuronidation allows cells from normal tissues to be protected from pan-RAS inhibition by ADT-007 despite the expectation that a pan-RAS inhibitor would be overtly toxic to the organism (39, 40). While UGT isozymes are well known to be expressed in metabolic tissues such as liver, colon, and kidney, they are also expressed in other normal tissues and regulated by multiple signaling pathways and transcription factors (41).

Regarding potential off-target effects of ADT-007, other indenes chemically related to ADT-007 were previously reported by Weinstein and colleagues to suppress cancer cell growth by a dual mechanism involving inhibition of cyclic guanine monophosphate phosphodiesterase (cGMP PDE) activity and tubulin polymerization (28). The latter was based on chemical resemblance of certain indenes with a trimethoxy moiety (e.g., ADT-106 as shown in **Supplemental Figure 4B**) to colchicine, which is well recognized in the field to inhibit tubulin polymerization (42). However, ADT-007 only affected tubulin polymerization and cGMP PDE activity (not shown) at concentrations appreciably higher than growth $IC_{50}$ values and did not

bind PDE10, a cGMP degrading PDE isozyme, as determined by CETSA experiments. These results lead us to conclude that neither inhibition of tubulin polymerization nor cGMP PDE activity account for the high potency or selectivity of ADT-007 as observed in growth and other assays. Previous reports showing that tubulin inhibitors induce MAPK pathway activity (43) rather than inhibit MAPK signaling lend further support to this conclusion. Nonetheless, the potential that ADT-007 inhibits tubulin polymerization at high dosages, along with its unique mechanism of metabolic deactivation allowing normal cells with high UGT levels to be protected from cytotoxicity, may be an additional therapeutic advantage given that tubulin is a well validated anticancer target. It is, however, noteworthy, that neither colchicine nor the topoisomerase inhibitor, etoposide, which has the same phenolic OH moiety as ADT-007, displayed selectivity for cancer cells with mutant RAS (not shown), suggesting a high degree of chemical specificity for the anticancer activity of ADT-007 highlighting its unique mechanism of action.

**ADT-007 inhibits a wide range of RAS-addicted tumors and circumvents resistance involving reactivation of the RAS pathway**

ADT-007 exhibited broad anticancer activity for mutant K/H/NRAS isozymes to inhibit downstream MAPK/AKT signaling critical for the proliferation and survival of cancer cells resulting in cell cycle arrest and apoptosis that would not be expected of pan-KRAS inhibitors or SOS1 blockers (44). The broad anticancer activity of ADT-007 supports its potential to be developed as a generalizable therapeutic for patients with PDA given that 94% of patients diagnosed with this malignancy have multiple KRAS mutations (25) and a significant proportion of patients with WT KRAS have RTK fusions that would be predicted to hyper-activate WT RAS isozymes (45). Furthermore, evidence indicates that ADT-007 exhibits high potency in tumor cells with activated RAS signaling, which may provide greater therapeutic utility in patients with metastatic disease in which proliferation of cancer cells is dependent upon activated KRAS signaling for survival in the metastatic niche (46). ADT-007 exhibits potent growth inhibition *in*

*vitro* and *in vivo* with syngeneic $KRAS^{G12D}$ mutated CRC and PDA cell lines and human $KRAS^{G12C}$ and $KRAS^{G12V}$ mutated PDA PDX models consistent with its pan-RAS inhibitory activity.

Equally important is the broad activity of ADT-007 with potential to provide second line therapy for patients with RAS mutant cancers that develop resistance to mutant-specific KRAS inhibitors. For NSCLC patients who develop resistance to $KRAS^{G12C}$-specific inhibitors, the majority of pathways that override sensitivity involve further activation of RAS signaling, including polyclonal mutations in RAS, co-occurring mutations in upstream receptor tyrosine kinases, or compensation from $RAS^{WT}$ isozymes (20, 47). Our findings indicate that ADT-007 maintains potency and growth inhibition in MIA PaCa-2 cells that develop resistance to mutant-specific KRAS inhibitors resulting from chronic exposure and in LLC lines with $KRAS^{G12C}$ $NRAS^{Q61H}$ dual mutations (26).

**ADT-007 modulates the tumor immune microenvironment**

Tumor growth inhibition by ADT-007 appears to be partially dependent upon the adaptive immune response as evidenced by reduced efficacy of ADT-007 on 2838c3 tumor cell growth in immune deficient Rag $1^{-/-}$ mice lacking B and T cells. Similar findings have been noted with $KRAS^{G12C}$ (18, 35) and $KRAS^{G12D}$-specific inhibitors (36), which demonstrated either that T cells contribute to the efficacy of targeted mutation-specific KRAS inhibitors or are critical for their long-term control of regrowth from metastatic disease (36). Furthermore, the presence of T cells predicted the response to PD-1 immune checkpoint blockade in preclinical models of NSCLC and PDA (35, 48, 49).

Despite this dependency, the impact of ADT-007 mediated inhibition of oncogenic $KRAS^{G12D}$ signaling, the impact on T cell numbers, activation, and function was variable and dependent upon the model system that requires further study. In both T cell inflamed, CT26 CRC and 7160c2 PDA tumor models, ADT-007 treatment displayed evidence of enhanced priming, activation, and functions of T cell subsets resulting in increased production of $T_H1$

cytokines including CCL2, IL-6, IL-2, TNFα, IFNγ, and the cytotoxic protein granzyme B. This was not observed in the 2838c3 model, which exhibited a higher basal state of T cell priming and activation than CT26 or 7160c2. Instead, T cell proportions, activation, and function were largely unaffected despite trends for increase in granzyme B and polyfunctional IL-2$^{+}$ IFNg$^{+}$ granzyme B$^{+}$ T cells (not shown). This data suggests that these models reflect different levels of activation of T cells most notably in 2838c3 model system, which has considerably more putative neoantigens than 7160c2 and increased proportion of CD103$^{+}$ DCs (34). Diversity within KPC tumor clones is attributed in part to epigenetic patterns of gene expression, such as CXCL-1, which in turn influence the composition and function of immune cells in the TME, has been noted and can also impact growth responses to immune checkpoint blockade (34, 48, 49). Although these differences are more pronounced between models and those with evidence of increased T cell infiltration and function, it is likely that myeloid and T cell responses will vary among preclinical tumor models due to variations in tumor epigenetics that impact the local immune microenvironment (35, 36).

**Conclusion**

These findings support further development of ADT-007 analogs and/or prodrugs with oral bioavailability to treat patients with RAS driven cancers as an alternative to mutant specific KRAS inhibitors or pan-KRAS inhibitors approved or in development. We envision that such agents can be used as monotherapy, in combination with immunotherapy, or other target-directed (e.g., EGFR) inhibitors. Towards this goal, we have developed an orally bioavailable prodrug of ADT-007, coded as ADT-1004, that has shown strong and robust *in vivo* antitumor activity in multiple aggressive mouse PDA models involving cancer cell lines or patient-derived cancer cells. ADT-1004 appears to be well tolerated and represents an attractive development candidate for further assessment of safety to support clinical trials.

**Material and Methods:**

Mice: 8 week-old female C57BL/6 mice (000664), male and female NOD.Cg-*Prkdc*$^{scid}$ *Il2rg*$^{tm1Wjl}$/SzJ (NSG, 00557) and female B6.129S7-*Rag1*$^{tm1Mom}$/J (Rag 1$^{-/-}$, 02216) were purchased from Jackson Laboratory. Female B6.Ifng/Thy1.1 KI (IFN-γ.Thy1.1) and B6.Cg-Tg-IL2$^{tm1(eGFP)/Weav}$ (IL-2.GFP) knock-in cytokine reporter mice were kindly provided by Dr. Casey Weaver (University of Alabama at Birmingham, Birmingham, AL) (37). 6-8 week-old female athymic foxn1 nude mice were bred locally at Department of Comparative Medicine, Oslo University Hospital. Experiments were randomized, but not blinded. All animal experiments and procedures were performed under approved protocols in accordance with guidelines from the University's Institutional Animal Care & Use Committee (IACUC). For animal studies performed at OUH Institute for Cancer Research (Norwegian Radium Hospital, Oslo, Norway) all procedures and experiments involving animals were approved by the Norwegian Food Safety Authority (application ID #18209) and were conducted according to the recommendations of the European Laboratory Animals Science Association and the ARRIVE guidelines.

Cell lines and patient derived xenografts: Murine PDA cell lines were derived from tumor-bearing Kras$^{LSL-G12D/+}$;Trp53$^{LSL-R172H/+}$;Pdx1-Cre;Rosa26$^{YFP/YFP}$ (7160c2, 2838c3) and Kras$^{LSL-G12D/+}$;Trp53$^{L/+}$;Pdx1-Cre (5363) cultured in DMEM complete media as previously indicated (34). Human tumor cell lines (BxPC-3, AsPC-1, MIA PaCa-2, PANC-1, SW-1990, HT-29, HCT116, A-549, SW-480, MDA-MB-231, OVCAR-8, Hs578T, SK-MEL2, H-1299, OV-90, H-1975, U87-MG, SK-OV3), and the murine tumor lines (B16-F10 and Lewis Lung cancer) were purchased from ATCC and maintained according to ATCC guidelines. The normal lung epithelial cells (NHAEC) were purchased from Lonza and cultured using bronchial epithelial growth medium per the supplier's protocol. NCM-460 cells were obtained from InCell and maintained in medium/nutrient mixture with 10% FBS less than 12 passages, according to the supplier's protocol. The human gall bladder adenocarcinoma expressing KRAS$^{G12V}$ was derived from an 80-year-old male with previous history of pancreatic cancer. Originally diagnosed as PDA, the

tumor was reclassified as a gall bladder adenocarcinoma. This PDX model was serially passaged in NSG mice. The CRC PDX models were established by implanting peritoneal metastasis samples collected at the time of CRS-HIPEC in the peritoneal cavity of nude mice. The PMP-1 model was established from a patient with an appendiceal primary lesion, while PMCA-1 was from a patient with a primary mucinous rectal carcinoma (50, 51). The PC244 model was established from a peritoneal metastasis specimen from a 69-year-old female with a poorly differentiated mucinous adenocarcinoma of the cecum. Targeted next-generation sequencing of PC244 was performed as previously described (52)

For studies performed at UAB, all cell lines and PDX models were tested against an extended panel of excluded pathogens including mycoplasma prior to *in vivo* studies as mandated by UAB IACUC and ARP guidelines.

<u>Tumor cell transfections:</u> BxPC-3 and HT-29 cells were initially exposed to lentiviral particles containing a mutant HRAS$^{G12V}$ or *KRAS*$^{G12C}$ construct for 48 hours in a 6-well plate at 37°C in a humidified incubator with 5% carbon dioxide. The media was then removed and replenished with fresh media containing HA-*HRAS*$^{G12V}$ or HA-*KRAS*$^{G12C}$ lentiviral particles. After another 48 hours, the media was removed, and fresh media containing 5 µg/mL puromycin was added to the well. Surviving cells were expanded in a 10 cm dish, and expression of the construct was confirmed by WB with an HA tag antibody (Cell Signaling Technology).

The HEK 293FT (Invitrogen, # R70007) cell line was transfected with either pBabe-puro-HA-KRASG12C (Addgene, #58901) or pBabe-puro-Empty (Addgene, #1764) retroviral constructs along with pCL-10A1 retrovirus packaging vector (Novus Biologicals, # NBP2-29542). Following a 48-h incubation at 37°C, culture supernatants containing viral particles were collected and mixed with PEG-itTM (SBI, #LV810A-1) virus precipitation reagent (5X) followed by overnight incubation at 4°C. Thereafter, supernatants were centrifuged at 1500 Xg for 30 min and white pellets of retroviral particles containing either pBabe-puro-HA-KRAS G12C or pBabe-

puro-Empty retroviral construct were collected and resuspended in sterile PBS. BxPC-3 cells were transduced with retroviral particles in a 6-well plate using polybrene transfection reagent (EMD MIllipore, TR-1003-G) and incubated for 48 h at 37°C. Thereafter, media was replaced with fresh media containing 5 µg/mL puromycin. Surviving cells were selected, expanded, and confirmed for $KRAS^{G12C}$ expression by Western blotting using an HA tag antibody (Cell Signaling Technology).

*In vitro* stimulation and ADT-007 treatments: For 2D and 3D cell cultures, cells were incubated with increasing concentrations (0.1-10,000 nM) of ADT-007, AMG-510 (Selleck Chemicals, Houston, TX) or MRTX849 (Selleck Chemicals, Houston, TX) or vehicle (DMSO) for a period of 24-72 hours depending on the assay. In some experiments 10 ng of recombinant, mouse EGF (Gibco, Jenks, OK) was added 10 minutes prior to harvesting protein lysates from treated tumor cell lines to assess the impact of upstream receptor tyrosine kinase activation of RAS-MAPK/AKT signaling.

Cell growth assays: To determine growth $IC_{50}$ values, 5 x $10^3$ tumor cells were plated in triplicate in 96 well flat bottom plate and incubated with various concentrations of ADT-007 (0.1-10,000 nM) and cultured for 72-96 hours depending on cellular growth kinetics. At 72 hours, cells were processed according to the manufacturer's recommendations to assess intra-cellular ATP levels as a measure of cellular proliferation and viability using CellTiter-Glo (Promega, Madison, WI). Nonlinear dose-response curves showing the effects of compound concentration on growth inhibition were generated using GraphPad Prism.

Gene expression database analysis: Transcriptomic (RNAseq) data for most of the cell lines in Table 1 is publicly available in Cancer Cell Line Encyclopedia accessed via the DepMap Portal) (29). The Student's T-test was used to identify significant differences in 19,221 TPM+1 normalized transcripts between the two categories of cell lines. Due to the modest number of

resistant lines, a threshold of $p < 0.01$ was chosen, which identified 719 transcripts and was reduced to 254, unique transcripts expressed at least a 5-fold difference.

NMR Spectroscopy: Recombinant full length $KRAS^{WT}$, in 50 mM Tris-Citrate, pH 6.5, 50 mM NaCl, 10 mM β-mercaptoethanol, 5 mM $MgCl_2$, 20mM $CaCl_2$, was dialyzed for 12 hr at 4 ºC using 1 L buffer with the following conditions: 50 mM Tris-Citrate pH=6.5, 50 mM NaCl, 10 mM β-mercaptoethanol, and 10 mM EDTA to remove $Mg^{2+}$ from KRAS. A second Dialysis for 12 hr at 4 ºC was done using 1 L buffer with the following conditions: 50 mM Tris-Citrate pH=6.5, 50 mM NaCl, and 10 mM β-mercaptoethanol to remove EDTA and any excess $Mg^{2+}$. All dialysis was done using Slide-A-Lyzer dialysis cassettes, 2K MWCO. To record $^{1}H$-$^{15}N$ heteronuclear single quantum coherence (HSQC) NMR spectra of $Mg^{2+}$Free-KRAS we used 900 MHz Avance spectrometers (Bruker, Billerica, MA, USA), equipped with cryogenic probes. Each *NMR* experiment was performed at 25°C in 50 mM Tris-Citrate pH=6.5, 50 mM NaCl, 10 mM β-mercaptoethanol containing 10% $D_2O$. The chemical shift assignments were obtained from the Biological Magnetic Resonance Data Bank (BMRB) database (http://www.bmrb.wisc.edu) using the BMRB accession numbers: 18529, 25114, and 26635.

$$\Delta\delta_{NH} = \sqrt{\frac{(\Delta\delta^{1}H_N)^2 + (\frac{\Delta\delta^{15}N)^2}{25}}{2}}$$

Chemical shift perturbations (CSPs) higher than the sum of the average and 1 SD were deemed statistically significant.

Nucleotide Exchange Assays: The fluorescent GTP analog MANT-GTP was purchased from Millipore Sigma. For each reaction, 5 µL of 5 µM purified GDP-bound K-RAS in reaction buffer (40 mM Tris-HCl, 100 mM NaCl, 20 mM MgCl, 1 mg/mL BSA, pH 7.5) and 2.5 µL of 200 mM EDTA was added to a microcentrifuge tube to make a master mix. Water was used in place of EDTA in some reactions as a control for the release of GDP. A 7.5 µL volume of master mix per

well was added to a 384-well plate for each respective reaction. A 5 µL volume of compound at five times the desired concentration or vehicle in reaction buffer was added to each respective well. After 2.5 minutes for equilibration at 26°C in a Bio-Tek Synergy H4 microplate reader, 12.5 µL of 1.5 µM MANT-GTP in reaction buffer was added to each well for a final concentration of 750 nM MANT-GTP, 1 µM RAS, 20 mM EDTA, and the desired concentration of compound or vehicle. In the case of compound preincubation, the plate was incubated for 1 hour at 26°C prior to MANT-GTP addition. Fluorescence was measured at an excitation wavelength of 360 nm and an emission wavelength of 460 nm in a Bio-Tek Synergy H4 microplate reader. Kinetic curves were generated with GraphPad Prism.

Cellular Thermal Shift Assay: A CETSA was performed with HCT-116 and HT-29 cells grown in RPMI medium supplemented with 10% FBS. For an initial determination of the melting profile of PDE10 and KRAS, fresh cell lysate prepared in non-denaturing buffer was cleared via centrifugation at 5,000 rpm for 15 min. Cleared lysate was dispensed into 96-well PCR (equivalent of approx. 6000 cells/well/50 µl), then was subjected to temperature gradient (38-65°C) for 10 min. Subsequently, centrifugation was performed at 14,000 rpm to sediment the unstable protein content. Supernatant was collected, SDS-PAGE gel was run, and immuno-detection was performed for KRAS and PDE10 (not shown) using corresponding primary antibodies. Band intensity was quantified on LI-COR C-Digit Blot Scanner, and subsequently $T_{agg}(50)$ and $T_{agg}(75)$ values were calculated for each protein. In a subsequent run, fresh lysates of HCT-116 and HT-29 cells were treated at various doses (0.06-1000 nM) of ADT-007, together with DMSO control, for 4 hours at 4C. Samples were then subjected to heat shock at 55C for 15 min, and unstable protein was separated by centrifugation step. Following an immuno-blotting analysis of the soluble fraction, bands of stable KRAS or PDE10 were quantified, normalized to DMSO, and plotted using GraphPad Prism software. Non-linear

regression analysis was used to fit a Sigmoidal dose-response curve with variable slope to generate $EC_{50}$ values for in-cell target engagement for the compounds.

Micro-tag in-cell binding assay: Another variation of the CETSA was performed using the NERD BIO Micro-Tag enzyme complementation method. A KRAS G12C Micro-Tag construct was engineered having a 15-amino acid tag at the N-terminus. The construct was transiently expressed in HEK293 cells. Two days post-transfection cells were lifted, washed with Tris Buffered Saline (TBS: 20mM Tris HCl pH7.4, 150mM NaCl) and re-suspended at 1000 cells/µl in TBS and 50,000 cells aliquoted to wells of a PCR plate. Increasing concentrations of ADT-007 were added and incubated with cells for 45 minutes, followed by heating for 10 min at 55°C, and a 1-minute cool down on ice. An equal volume of 0.5% Triton-X-100 in TBS was added, and cells lysed for 10 min on ice followed by addition of the Tag binding protein and substrate and immediately proceeded to measurement of fluorescence signal. Fluorescence signal was plotted with concentration of the compounds on a semi-log scale using GraphPad Prism 9.0 software.

RAS Activation Assay: Cells were grown to 80 percent confluence using complete growth medium, then washed with 1 mL of PBS and lysed on ice for 5 min, (25 mM Tris HCl, 150 mM NaCl, 5 mM $MgCl_2$, 1% NP-40, 5% glycerol, pH 7.2) with Halt Protease and Phosphatase Inhibitor Cocktail (Thermo Fisher Scientific), and clarified at 16,000 RCF 15 minutes at 4°C. Protein concentration of the supernatant was normalized using the DC protein assay (Bio-Rad). Whole cell lysates (200 µg) were incubated with GST-RAF-RBD (Addgene) bound to glutathione agarose beads at 4°C for 1 hour. Bound active RAS was collected by centrifugation at 6,000 RCF for 30 seconds at 4°C, washed thrice with lysis buffer, then eluted with SDS sample buffer, and subsequently detected by Western blotting with a pan-RAS antibody or isozyme specific antibody as described below.

Western blotting: Tumor or cell lysates were generated after treatment with 500 uL RIPA lysis buffer (Thermo Scientific, 89900) with protease and phosphatase inhibitors (Thermo Scientific, 78440), boiled for 5 minutes and equal protein concentrations were loaded and separated by SDS-PAGE on a 12% gel. Gels were transferred to a PVDF membrane, which were blocked with either 5% non-fat dry milk in TBS-T (TBS with 0.1% Tween 20) or 5% BSA in TBS-T, depending on the blocking agent used for the primary antibodies, for 1 hour at room temperature. Membranes were incubated overnight at 4°C on a rocker with primary antibodies **(Supplemental Table 2**) according to the manufacturer's instructions and then developed with HRP-conjugated secondary antibodies (Cell Signaling Technology) for 1 hour at room temperature on an orbital shaker. Membranes were developed using SuperSignal West Enhanced Chemiluminescent substrate (Thermo Fisher Scientific) and imaged using a ChemiDoc Imaging System (Bio-Rad).

Tumor cell implantation and ADT-007 treatment: A single cell suspension of murine CRC or PDA cells was prepared PBS and kept on ice until injection. $1x10^6$ syngeneic mouse CRC and PDA tumor cells were injected subcutaneously into 6–8-week-old BALB/C or C57BL/6 mice respectively. When tumors reached an average tumor volume of 150 $mm^3$ mice began receiving daily intra-tumoral (10 mg/kg, QD, 7 days/week for 17-21 days) or peri-tumoral (5 mg/kg, BID, 7 days/week for 17-21 days). Tumor growth was assessed by caliper measurements (2-3/week) and tumor volumes ($TV = W \times L^2/2$) were calculated throughout the study. No overt signs of toxicity (body weight loss or organ [lungs, heart, liver, GI tract] pathology) were noted with local administration.

Flow Cytometry: Mouse tumors were digested in a 1 mg/mL collagenase IV and 0.1 mg/mL DNSase 1 (Worthington Biochemical, Lakewood, NJ) in HBSS for 45 minutes at 37 °C with intermittent shaking. Samples were then washed with RPMI containing 10% FBS and filtered through a 70μM strainer generating single cell suspensions. Cells were labeled with primary

fluorophore-conjugated antibodies and a live/dead stain (**Supplemental Table 3**) for 30-60 min at 4 °C, washed and re-suspended in flow buffer. Cytokine expression from single cell suspensions of spleen and tumor was quantified as follows: cells were plated at a concentration of $10^6$ cells in 1 mL of RP-10 media and stimulated for 5 hours at 37°C using a 1x solution of a Cell Activation Cocktail containing PMA ionomycin, and Brefeldin A (Biolegend, San Diego, CA). Conversely, cells were cultured for 5 hours at 37°C using a solution containing 5 ug of Brefeldin A (BioLegend, San Diego, CA) to serve as an unstimulated control. After cell surface staining, cells were fixed in 4% paraformaldehyde for 45 minutes at 4 °C then washed with 1x Perm/Wash (BD, 554723). For intracellular staining in tumor and spleen samples, cells were stained with an antibody cocktail specific intracellular cytokines (IL-2, IFNγ, TNFα, and granzyme B) in Perm/Wash solution for 60 minutes at 4 °C. Data were acquired on a Symphony A5 flow cytometer, with analysis performed using FlowJo version 10.7.2.

Statistical Analyses: GraphPad Prism (version 9.1.2) was used for statistical analyses and graphical representation with data are presented as either means ± standard deviation (SD) or standard error of the mean (SEM). Two-tailed Student's t-test and Two-way Analysis of Variance (ANOVA) with multiple corrections (Bonnferoni method) were performed for determination of statistical significance between groups. For $IC_{50}$ generation, concentrations were log transformed, data were then normalized to control and *log*(inhibitor) vs. response (four parameter nonlinear dose-response) test was used. A $p < 0.05$ was considered statistically significant.

**Acknowledgements**:

Thanks to Dr. Ajay Singh for editorial help and Dr. Haseeb Zubair for technical assistance. Thanks to Dr. Asfar Azmi for providing the MRTX-1257-resistant cells. Thanks to Mr. Bernard D. Gary, Dr. Kevin J. Lee, Dr. Sara C. Sigler, Dr. M. Kate Saville, Dr. Joel F. Andrews, and Dr. Bing Zhu for technical assistance insightful discussions.

## References:


1. Siegel RL, Miller KD, Fuchs HE, Jemal A. Cancer statistics, 2022. CA Cancer J Clin. 2022;72(1):7-33.
2. Yang Y, Zhang H, Huang S, Chu Q. KRAS Mutations in Solid Tumors: Characteristics, Current Therapeutic Strategy, and Potential Treatment Exploration. J Clin Med. 2023;12(2).
3. Hingorani SR, Petricoin EF, Maitra A, Rajapakse V, King C, Jacobetz MA, et al. Preinvasive and invasive ductal pancreatic cancer and its early detection in the mouse. Cancer Cell. 2003;4(6):437-50.
4. Kojima K, Vickers SM, Adsay NV, Jhala NC, Kim HG, Schoeb TR, et al. Inactivation of Smad4 accelerates Kras(G12D)-mediated pancreatic neoplasia. Cancer Res. 2007;67(17):8121-30.
5. Boutin AT, Liao WT, Wang M, Hwang SS, Karpinets TV, Cheung H, et al. Oncogenic Kras drives invasion and maintains metastases in colorectal cancer. Genes Dev. 2017;31(4):370-82.
6. Bardeesy N, Aguirre AJ, Chu GC, Cheng KH, Lopez LV, Hezel AF, et al. Both p16(Ink4a) and the p19(Arf)-p53 pathway constrain progression of pancreatic adenocarcinoma in the mouse. Proc Natl Acad Sci U S A. 2006;103(15):5947-52.
7. Ying H, Kimmelman AC, Lyssiotis CA, Hua S, Chu GC, Fletcher-Sananikone E, et al. Oncogenic Kras maintains pancreatic tumors through regulation of anabolic glucose metabolism. Cell. 2012;149(3):656-70.
8. Mukhopadhyay S, Goswami D, Adiseshaiah PP, Burgan W, Yi M, Guerin TM, et al. Undermining Glutaminolysis Bolsters Chemotherapy While NRF2 Promotes Chemoresistance in KRAS-Driven Pancreatic Cancers. Cancer Res. 2020;80(8):1630-43.
9. Collins MA, Brisset JC, Zhang Y, Bednar F, Pierre J, Heist KA, et al. Metastatic pancreatic cancer is dependent on oncogenic Kras in mice. PLoS One. 2012;7(12):e49707.
10. Zhang Y, Yan W, Collins MA, Bednar F, Rakshit S, Zetter BR, et al. Interleukin-6 is required for pancreatic cancer progression by promoting MAPK signaling activation and oxidative stress resistance. Cancer Res. 2013;73(20):6359-74.
11. Zdanov S, Mandapathil M, Abu Eid R, Adamson-Fadeyi S, Wilson W, Qian J, et al. Mutant KRAS Conversion of Conventional T Cells into Regulatory T Cells. Cancer immunology research. 2016;4(4):354-65.
12. Bayne LJ, Beatty GL, Jhala N, Clark CE, Rhim AD, Stanger BZ, et al. Tumor-derived granulocyte-macrophage colony-stimulating factor regulates myeloid inflammation and T cell immunity in pancreatic cancer. Cancer Cell. 2012;21(6):822-35.
13. Ischenko I, D'Amico S, Rao M, Li J, Hayman MJ, Powers S, et al. KRAS drives immune evasion in a genetic model of pancreatic cancer. Nat Commun. 2021;12(1):1482.
14. Coelho MA, de Carne Trecesson S, Rana S, Zecchin D, Moore C, Molina-Arcas M, et al. Oncogenic RAS Signaling Promotes Tumor Immunoresistance by Stabilizing PD-L1 mRNA. Immunity. 2017;47(6):1083-99 e6.
15. Muthalagu N, Monteverde T, Raffo-Iraolagoitia X, Wiesheu R, Whyte D, Hedley A, et al. Repression of the Type I Interferon Pathway Underlies MYC- and KRAS-Dependent Evasion of NK and B Cells in Pancreatic Ductal Adenocarcinoma. Cancer Discov. 2020;10(6):872-87.
16. Stalnecker CA, Der CJ. RAS, wanted dead or alive: Advances in targeting RAS mutant cancers. Sci Signal. 2020;13(624).
17. Kwan AK, Piazza GA, Keeton AB, Leite CA. The path to the clinic: a comprehensive review on direct KRAS(G12C) inhibitors. J Exp Clin Cancer Res. 2022;41(1):27.
18. Canon J, Rex K, Saiki AY, Mohr C, Cooke K, Bagal D, et al. The clinical KRAS(G12C) inhibitor AMG 510 drives anti-tumour immunity. Nature. 2019;575(7781):217-23.

833 19. Ryan MB, Fece de la Cruz F, Phat S, Myers DT, Wong E, Shahzade HA, et al. Vertical Pathway
834 Inhibition Overcomes Adaptive Feedback Resistance to KRAS(G12C) Inhibition. Clinical cancer research :
835 an official journal of the American Association for Cancer Research. 2020;26(7):1633-43.
836 20. Awad MM, Liu S, Rybkin, II, Arbour KC, Dilly J, Zhu VW, et al. Acquired Resistance to KRAS(G12C)
837 Inhibition in Cancer. N Engl J Med. 2021;384(25):2382-93.
838 21. Thompson HJ, Jiang C, Lu J, Mehta RG, Piazza GA, Paranka NS, et al. Sulfone metabolite of
839 sulindac inhibits mammary carcinogenesis. Cancer Res. 1997;57(2):267-71.
840 22. Herrmann C, Block C, Geisen C, Haas K, Weber C, Winde G, et al. Sulindac sulfide inhibits Ras
841 signaling. Oncogene. 1998;17(14):1769-76.
842 23. Karaguni IM, Glusenkamp KH, Langerak A, Geisen C, Ullrich V, Winde G, et al. New indene-
843 derivatives with anti-proliferative properties. Bioorg Med Chem Lett. 2002;12(4):709-13.
844 24. Piazza GA, Keeton AB, Tinsley HN, Gary BD, Whitt JD, Mathew B, et al. A novel sulindac
845 derivative that does not inhibit cyclooxygenases but potently inhibits colon tumor cell growth and
846 induces apoptosis with antitumor activity. Cancer Prev Res (Phila). 2009;2(6):572-80.
847 25. Waters AM, Der CJ. KRAS: The Critical Driver and Therapeutic Target for Pancreatic Cancer. Cold
848 Spring Harb Perspect Med. 2018;8(9).
849 26. Molina-Arcas M, Moore C, Rana S, van Maldegem F, Mugarza E, Romero-Clavijo P, et al.
850 Development of combination therapies to maximize the impact of KRAS-G12C inhibitors in lung cancer.
851 Sci Transl Med. 2019;11(510).
852 27. Tanaka N, Lin JJ, Li C, Ryan MB, Zhang J, Kiedrowski LA, et al. Clinical Acquired Resistance to
853 KRAS(G12C) Inhibition through a Novel KRAS Switch-II Pocket Mutation and Polyclonal Alterations
854 Converging on RAS-MAPK Reactivation. Cancer Discov. 2021;11(8):1913-22.
855 28. Xiao D, Deguchi A, Gundersen GG, Oehlen B, Arnold L, Weinstein IB. The sulindac derivatives
856 OSI-461, OSIP486823, and OSIP487703 arrest colon cancer cells in mitosis by causing microtubule
857 depolymerization. Mol Cancer Ther. 2006;5(1):60-7.
858 29. Barretina J, Caponigro G, Stransky N, Venkatesan K, Margolin AA, Kim S, et al. The Cancer Cell
859 Line Encyclopedia enables predictive modelling of anticancer drug sensitivity. Nature.
860 2012;483(7391):603-7.
861 30. Lee KJ, Chang WL, Chen X, Valiyaveettil J, Ramirez-Alcantara V, Gavin E, et al. Suppression of
862 Colon Tumorigenesis in Mutant Apc Mice by a Novel PDE10 Inhibitor that Reduces Oncogenic β-Catenin.
863 Cancer Prev Res (Phila). 2021;14(11):995-1008.
864 31. John J, Rensland H, Schlichting I, Vetter I, Borasio GD, Goody RS, et al. Kinetic and structural
865 analysis of the Mg(2+)-binding site of the guanine nucleotide-binding protein p21H-ras. The Journal of
866 biological chemistry. 1993;268(2):923-9.
867 32. Hunter JC, Manandhar A, Carrasco MA, Gurbani D, Gondi S, Westover KD. Biochemical and
868 Structural Analysis of Common Cancer-Associated KRAS Mutations. Molecular cancer research : MCR.
869 2015;13(9):1325-35.
870 33. Agola JO, Hong L, Surviladze Z, Ursu O, Waller A, Strouse JJ, et al. A competitive nucleotide
871 binding inhibitor: in vitro characterization of Rab7 GTPase inhibition. ACS chemical biology.
872 2012;7(6):1095-108.
873 34. Li J, Byrne KT, Yan F, Yamazoe T, Chen Z, Baslan T, et al. Tumor Cell-Intrinsic Factors Underlie
874 Heterogeneity of Immune Cell Infiltration and Response to Immunotherapy. Immunity. 2018;49(1):178-
875 93 e7.
876 35. Mugarza E, van Maldegem F, Boumelha J, Moore C, Rana S, Llorian Sopena M, et al. Therapeutic
877 KRAS(G12C) inhibition drives effective interferon-mediated antitumor immunity in immunogenic lung
878 cancers. Sci Adv. 2022;8(29):eabm8780.

879 36. Kemp SB, Cheng N, Markosyan N, Sor R, Kim IK, Hallin J, et al. Efficacy of a Small-Molecule
880 Inhibitor of KrasG12D in Immunocompetent Models of Pancreatic Cancer. Cancer Discov.
881 2023;13(2):298-311.
882 37. Harrington LE, Janowski KM, Oliver JR, Zajac AJ, Weaver CT. Memory CD4 T cells emerge from
883 effector T-cell progenitors. Nature. 2008;452(7185):356-60.
884 38. Khan I, Koide A, Zuberi M, Ketavarapu G, Denbaum E, Teng KW, et al. Identification of the
885 nucleotide-free state as a therapeutic vulnerability for inhibition of selected oncogenic RAS mutants. Cell
886 Rep. 2022;38(6):110322.
887 39. Esteban LM, Vicario-Abejon C, Fernandez-Salguero P, Fernandez-Medarde A, Swaminathan N,
888 Yienger K, et al. Targeted genomic disruption of H-ras and N-ras, individually or in combination, reveals
889 the dispensability of both loci for mouse growth and development. Mol Cell Biol. 2001;21(5):1444-52.
890 40. Johnson L, Greenbaum D, Cichowski K, Mercer K, Murphy E, Schmitt E, et al. K-ras is an essential
891 gene in the mouse with partial functional overlap with N-ras. Genes Dev. 1997;11(19):2468-81.
892 41. Allain EP, Rouleau M, Lévesque E, Guillemette C. Emerging roles for UDP-
893 glucuronosyltransferases in drug resistance and cancer progression. Br J Cancer. 2020;122(9):1277-87.
894 42. Lu Y, Chen J, Xiao M, Li W, Miller DD. An overview of tubulin inhibitors that interact with the
895 colchicine binding site. Pharm Res. 2012;29(11):2943-71.
896 43. Waters AM, Khatib TO, Papke B, Goodwin CM, Hobbs GA, Diehl JN, et al. Targeting p130Cas- and
897 microtubule-dependent MYC regulation sensitizes pancreatic cancer to ERK MAPK inhibition. Cell Rep.
898 2021;35(13):109291.
899 44. Coley AB, Ward A, Keeton AB, Chen X, Maxuitenko Y, Prakash A, et al. Pan-RAS inhibitors: Hitting
900 multiple RAS isozymes with one stone. Adv Cancer Res. 2022;153:131-68.
901 45. Luchini C, Paolino G, Mattiolo P, Piredda ML, Cavaliere A, Gaule M, et al. KRAS wild-type
902 pancreatic ductal adenocarcinoma: molecular pathology and therapeutic opportunities. J Exp Clin
903 Cancer Res. 2020;39(1):227.
904 46. di Magliano MP, Logsdon CD. Roles for KRAS in pancreatic tumor development and progression.
905 Gastroenterology. 2013;144(6):1220-9.
906 47. Sheffels E, Kortum RL. The Role of Wild-Type RAS in Oncogenic RAS Transformation. Genes
907 (Basel). 2021;12(5).
908 48. Mahadevan KK, McAndrews KM, LeBleu VS, Yang S, Lyu H, Li B, et al. KRAS(G12D) inhibition
909 reprograms the microenvironment of early and advanced pancreatic cancer to promote FAS-mediated
910 killing by CD8(+) T cells. Cancer Cell. 2023;41(9):1606-20 e8.
911 49. Mahadevan KK, McAndrews KM, LeBleu VS, Yang S, Lyu H, Li B, et al. Oncogenic Kras (G12D)
912 specific non-covalent inhibitor reprograms tumor microenvironment to prevent and reverse early pre-
913 neoplastic pancreatic lesions and in combination with immunotherapy regresses advanced PDAC in a
914 CD8 (+) T cells dependent manner. bioRxiv. 2023.
915 50. Flatmark K, Reed W, Halvorsen T, Sorensen O, Wiig JN, Larsen SG, et al. Pseudomyxoma
916 peritonei--two novel orthotopic mouse models portray the PMCA-I histopathologic subtype. BMC
917 Cancer. 2007;7:116.
918 51. Flatmark K, Davidson B, Kristian A, Stavnes HT, Førsund M, Reed W. Exploring the peritoneal
919 surface malignancy phenotype—a pilot immunohistochemical study of human pseudomyxoma peritonei
920 and derived animal models. Human Pathology. 2010;41(8):1109-19.
921 52. Fleten KG, Lund-Andersen C, Waagene S, Abrahamsen TW, Mørch Y, Boye K, et al. Experimental
922 Treatment of Mucinous Peritoneal Metastases Using Patient-Derived Xenograft Models. Translational
923 oncology. 2020;13(8):100793.

924

925

**Figures and legends:**

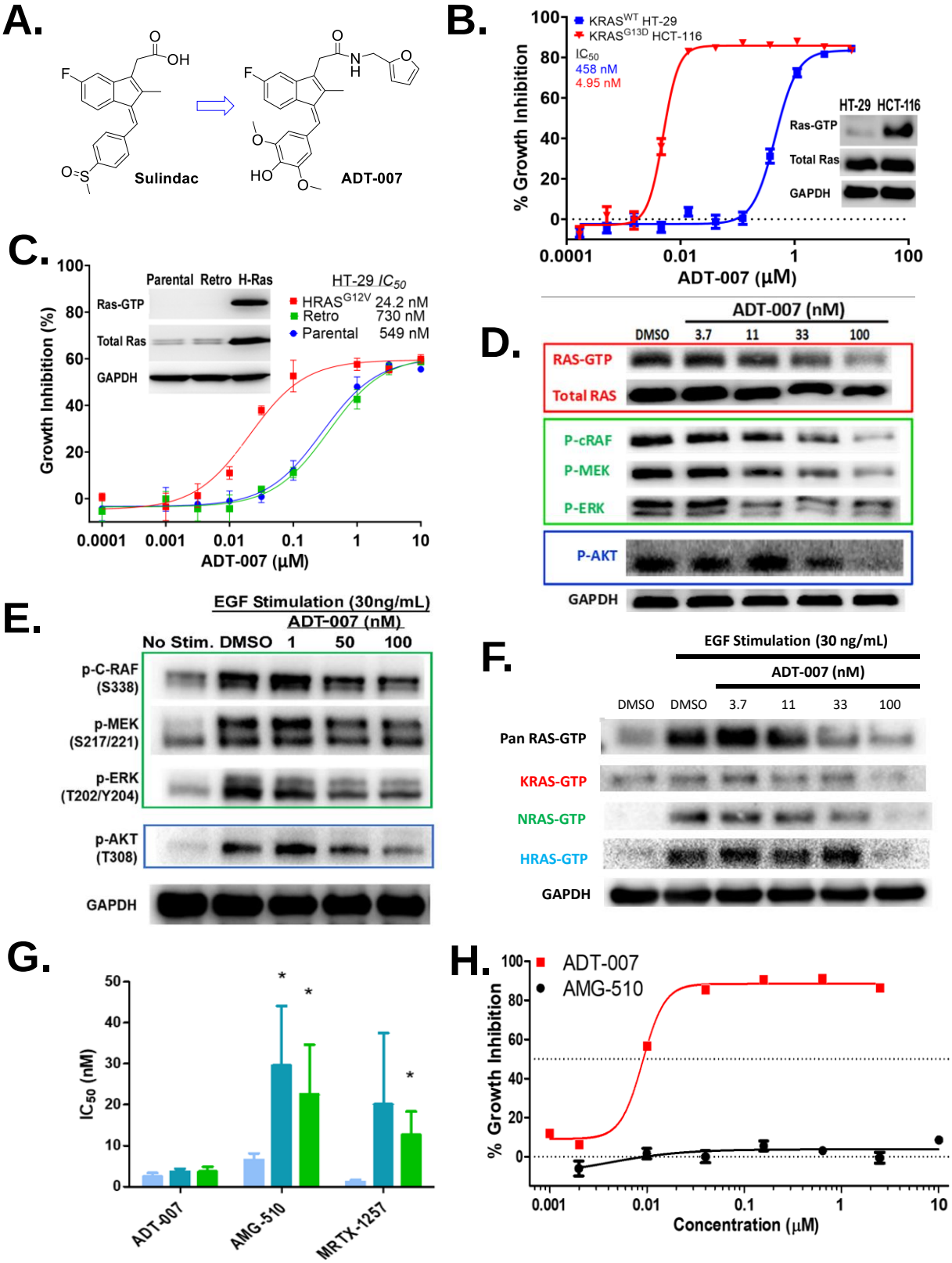

**Figure 1. ADT-007 inhibits mutant RAS and EGF activation of RAS$^{WT}$ isozymes and downstream MAPK signaling to circumvent resistance. (A)** Chemical structure of ADT-007. **(B)** ADT-007 potently and selectively inhibits growth of mutant KRAS$^{G13D}$ HCT-116 (red) compared to KRAS$^{WT}$, BRAF$^{V600}$ mutant HT-29 (blue) following 72 hours of treatment (Cell Titer Glo Assay)**.** Each concentration of ADT-007 was tested in quadruplicate to generate a sigmoidal curve. Error bars represent standard error of the mean (SEM). Inset: Activated RAS-GTP measured by RAS-RBD pull-down assays followed by WB using a pan-RAS antibody. Total RAS and GAPDH were evaluated by WB **(C)** Ectopic expression of HRAS$^{G12V}$ in HT-29 cells renders cells sensitive to ADT-007-mediated growth inhibition following 72 hours of treatment (Cell Titer Glo Assay). Samples were run in quadruplicate. Error bars represent SEM. Inset: Activated (GTP-RAS), total RAS, and GAPDH. **(D)** KRAS$^{G13D}$ mutant HCT-116 cells were treated overnight in serum free media with increasing concentrations of ADT-007. GTP RAS levels were measured by RAS-RBD pull-down assays followed by WB using a pan-RAS antibody. Phosphorylated RAF, MEK, ERK, AKT, and total RAS and GAPDH were evaluated from protein lysates by WB. Data is representative of 3 independent experiments. **(E)** KRAS$^{G12C}$ mutant MIA Paca-2 cells were treated overnight in serum free media with increasing concentrations of ADT-007 and then stimulated for 10 min with EGF (30 ng/mL). Phosphorylated RAF, MEK, ERK, AKT and total RAS and GAPDH were evaluated from protein lysates by WB. Data is representative of 3 independent experiments. **(F)** KRAS$^{G12C}$ mutant MIA PaCa-2 cells were treated with vehicle (DMSO) or ADT-007 for 24 hours in serum-free media and then stimulated with 30 ng/mL EGF for 10 minutes. Activated (GTP-RAS) was measured by RAS-RBD pull-down assays followed by WB using pan-RAS or KRAS, HRAS, and NRAS specific antibodies. Results shown are representative of at least two independent experiments demonstrating effects observed on RAS isozymes. **(G)** Growth inhibitory activity of ADT-007 and mutant G12C KRAS inhibitors, AMG-510 and MRTX 1257, in parental or resistant MIA PaCa-2 cells. Data is representative triplicates of 3 independent experiments. p values (* p <

0.05) were determined by the Student's unpaired t-test, ns indicates not significant. Error bars indicate SEM. (**H**) Murine Lewis Lung Cancer cells harboring both KRAS-G12C and NRAS-Q61H mutations were sensitive to ADT-007 but not AMG-510. Data is representative of 2 experiments. Error bars indicate SEM.

| Type | Tissue Origin | Cell Line | Mutation Status | $IC_{50}$ (nM) | UGT1A10 mRNA |
|---|---|---|---|---|---|
| Mutant RAS, sensitive | Pancreatic | MIA PaCa-2 | KRAS G12C | 2.1 | 0.263 |
| | Pancreatic | PANC-1 | KRAS G12D | 2.4 | 0.043 |
| | Pancreatic | SW-1990 | KRAS G12D | 6.3 | 0.138 |
| | Lung | A549 | KRAS G12S | 6.8 | 0.070 |
| | Pancreatic | CFPAC-1 | KRAS G12V | 5.8 | 2.63 |
| | Colon | SW480 | KRAS G12V | 6.5 | 0.58 |
| | Breast | MDA-MB-231 | KRAS G13D | 3.6 | 0.043 |
| | Colon | HCT-116 | KRAS G13D | 4.7 | 0 |
| | Ovarian | OVCAR-8 | KRAS P121H | 5.8 | 0.057 |
| | Breast | Hs 578T | HRAS G12D | 3.9 | 0.098 |
| | Skin | SK-MEL-2 | NRAS Q61K | 2.1 | 0 |
| | Lung | NCI-H1299 | NRAS Q61K | 2.4 | 0 |
| WT RAS, resistant | Normal Lung | NHAEC | WT RAS | 19100 | * |
| | Normal Colon | NCM460 | WT RAS | > 25,000 | * |
| Downstream mutation (WT RAS) resistant | Ovarian | OV-90 | WT RAS/mut BRAF | 350 | 4.57 |
| | Colon | HT-29 | WT RAS/mut BRAF | 512 | 6.97 |
| | Skin | SK-MEL-28 | WT RAS/mut BRAF | > 25,000 | 0.14 (3.53†) |
| | Pancreatic | BxPC-3 | WT RAS/mut BRAF | 2500 | 7.75 |
| Upstream RAS activation sensitive | Lung | NCI-H1975 | WT RAS/mut EGFR | 3.9 | * |
| | Skin (mouse) | B16 | WT RAS/mut PDGFR | 5.8 | * |
| | Brain | U-87 MG | WT RAS/mut NF1 | 1.6 | 0 |
| | Ovarian | SK-OV-3 | WT RAS/mut NF1 | 6.7 | 0.202 |

**Table 1. Sensitivity of tumor cells to ADT-007 is associated with high activated RAS levels and low levels of UGT superfamily enzymes.** Growth inhibitory ($IC_{50}$) values were determined by ATP content using the Promega Cell Titer Glo assay following 72-96 hours of treatment. UGT1A10 mRNA levels are expressed as transcripts per million (TPM) to normalize expression of the most significant differentially expressed UGT isozyme from data published in the Cancer Cell Line Encyclopedia accessed via the DepMap Portal hosted by the Broad Institute. † TPM normalized expression of UGT2B7 in SK-MEL-28).

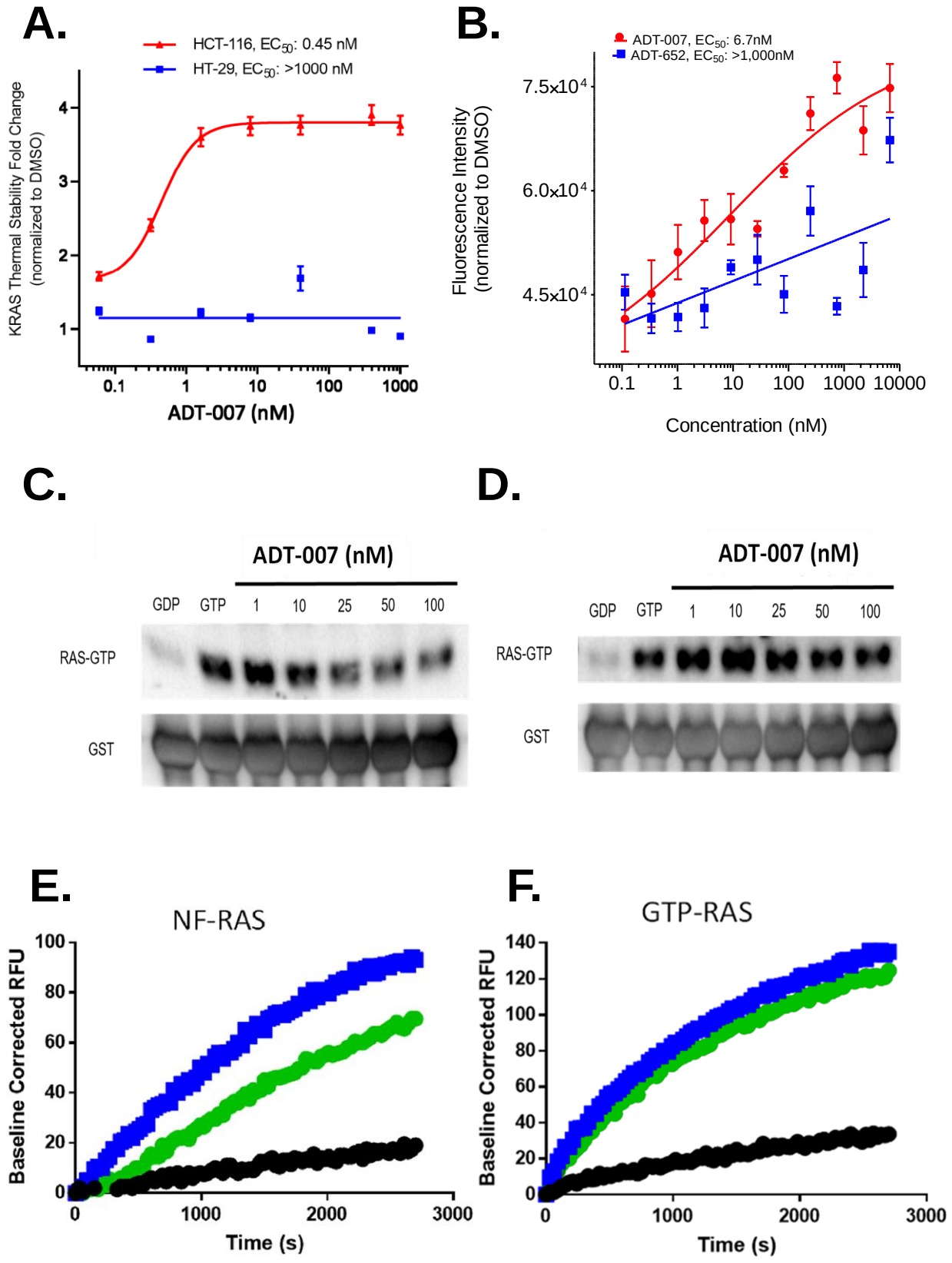
A.
HCT-116, EC50: 0.45 nM
HT-29, EC50: >1000 nM
KRAS Thermal Stability Fold Change (normalized to DMSO)
ADT-007 (nM)
B.
ADT-007, EC50: 6.7nM
ADT-652, EC50: >1,000nM
Fluorescence Intensity (normalized to DMSO)
Concentration (nM)
C.
ADT-007 (nM)
GDP
GTP
1
10
25
50
100
RAS-GTP
GST
D.
ADT-007 (nM)
GDP
GTP
1
10
25
50
100
RAS-GTP
GST
E.
NF-RAS
Baseline Corrected RFU
Time (s)
F.
GTP-RAS
Baseline Corrected RFU
Time (s)

966

**<u>Figure 2. ADT-007 binds KRAS, inhibits nucleotide loading and effector binding.</u> (A)** Cellular thermal shift assay (CETSA) shows ADT-007 binds KRAS with high affinity in mutant $KRAS^{G13D}$ HCT-116 but not $KRAS^{WT}$ HT-29 CRC cells. Graphs show levels of compound stabilized KRAS detected by WB compared with vehicle control. Data are representative of two independent experiments. (**B**) Binding affinity of ADT-007 for mutant $KRAS^{G12C}$ was assessed by 45 min treatment of HEK293 cells expressing KRAS G12C-Micro-Tag construct followed by cellular thermal shift assays in comparison with a negative control, ADT-652, a trimethoxy ADT-007 analog lacking selectivity. Curves are graphed as the average of two replicates ± SEM. **(C-D)** The inhibitory activity of ADT-007 to block recombinant $KRAS^{WT}$ binding to GTP in a cell free system was evaluated by RAS-RBD pull-down assays followed by WB. (**C**) ADT-007 inhibited $KRAS^{WT}$-RAF binding before GTP addition. **(D)** ADT-007 did not inhibit $KRAS^{WT}$ effector binding when added after GTP loading, but before the active KRAS pull-down. Data is representative of at least 3 independent experiments. (**E-F**) Kinetics of GTP binding to KRAS was measured using a fluorescent GTP analog (Mant-GTP). ADT-007 reduced the rate of GTP binding to KRAS if pretreated with EDTA to chelate $Mg^{2+}$. (**E**), but not if added after adding non-hydrolysable GTPγS **(F)** prior to incubation with ADT-007. Data is representative of at least three independent experiments.

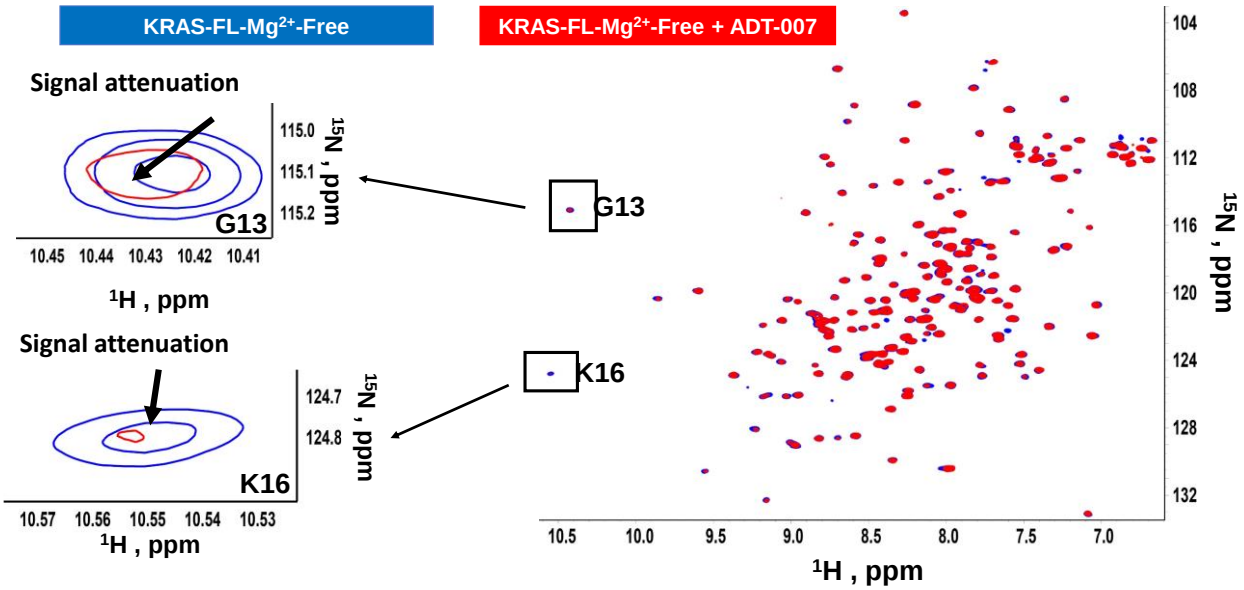


**<u>Figure 3. NMR analysis of ADT-007 binding to KRAS.</u>** Addition of 125 µM ADT-007 (red) to 25 µM $Mg^{2+}$-free KRAS (blue) resulted in statistically significant NMR signal attenuation at G13 and K16 and other residues. Assignments for G13 and K16 due to their unique resonance frequencies are shown as a larger image to the left.

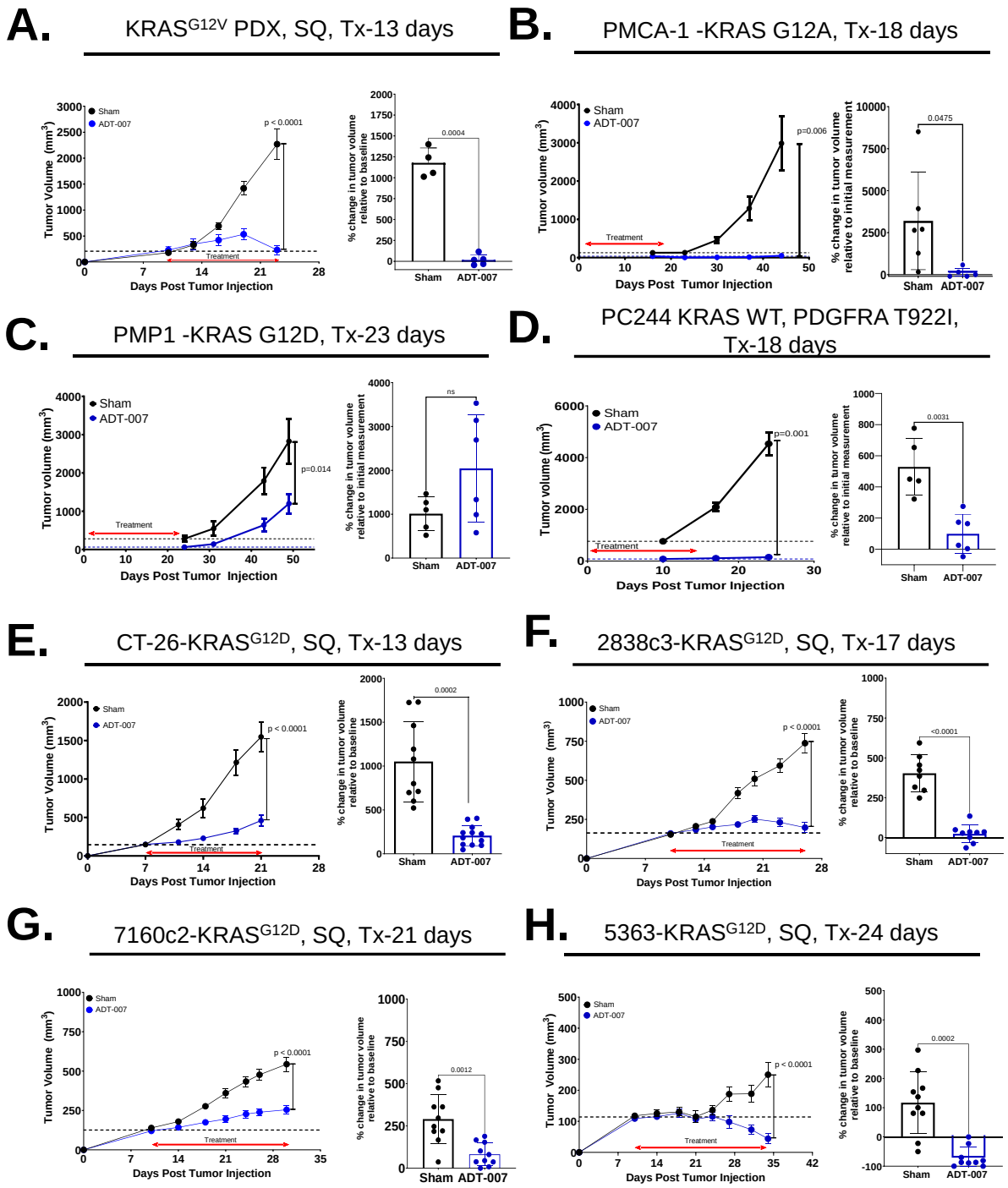


**<u>Figure 4. ADT-007 induces growth arrest and regression of CRC, GBA, and PDA cells *in vivo*.</u>** (**A**) Left panel: Growth inhibition of subcutaneous patient derived xenograft (PDX) gall bladder adenocarcinoma (GBA) bearing KRAS$^{G12V}$ by peritumoral administration (5 mg/kg, BID, 13 days, n = 5 mice/group, $p < 0.0001$, mean ± SEM). Right panel: Percent change in tumor

size at endpoint compared to size at start of treatment. (**B**-**D**) Left panels: Growth inhibition of peritoneal metastasis models of mucinous colorectal adenocarcinoma models (**B**) PMCA1, (**C**) PMP1, and (**D**) PC244 in nude mice by IP administration of ADT-007 (2.5 mg/kg, BID) for treatment periods of 18 (PMCA1), 23 (PMP1), and 18 days (PC244). Treatment was initiated 24 hours after implantation (n = 5-6 mice/group, mean ± SE) and mice were followed for a period of 24 to 50 days (6 – 31 days post treatment cessation) after implantation by MRI. Right panels: tumor sizes at end of treatment. (**E**) Left panel: Growth inhibition of subcutaneous CT26 colon tumors in BALB/c mice by IT administration of ADT-007 (10 mg/kg, QD, 13 days) (** $p<0.001$, **** $p<0.0001$, mean ± SE, n=12). Right panel: Percent change in tumor size at endpoint compared to size at start of treatment. (**F-H**) Left panels: Growth inhibition studies of subcutaneous (**F**) 2838c3, (**G**) 7160c2, (**H**) 5363 PDA tumors in C57BL/6 mice by peritumoral administration of ADT-007 (5 mg/kg, BID) for treatment periods of 17 (2838c3), 20 (7160c2), and 24 (5363) days respectively after implantation (n = 7 – 10 mice/group, $p <0.0001$, mean ± SE). Right Panels: Percent change in tumor size at endpoint compared to size at start of treatment. All animal studies are representative of 2-3 independent experiments. Growth kinetics and animal health status (ulceration) determined endpoints for each study. Left panels: Error bars for left panels are representative of SEM. Right panels: error bars are representative of SD. Left panels: Statistical significance was assessed using 2-way ANOVA with Sadik's multiple comparisons test. Right panels: Statistical significance was assessed with Welch's t-test.

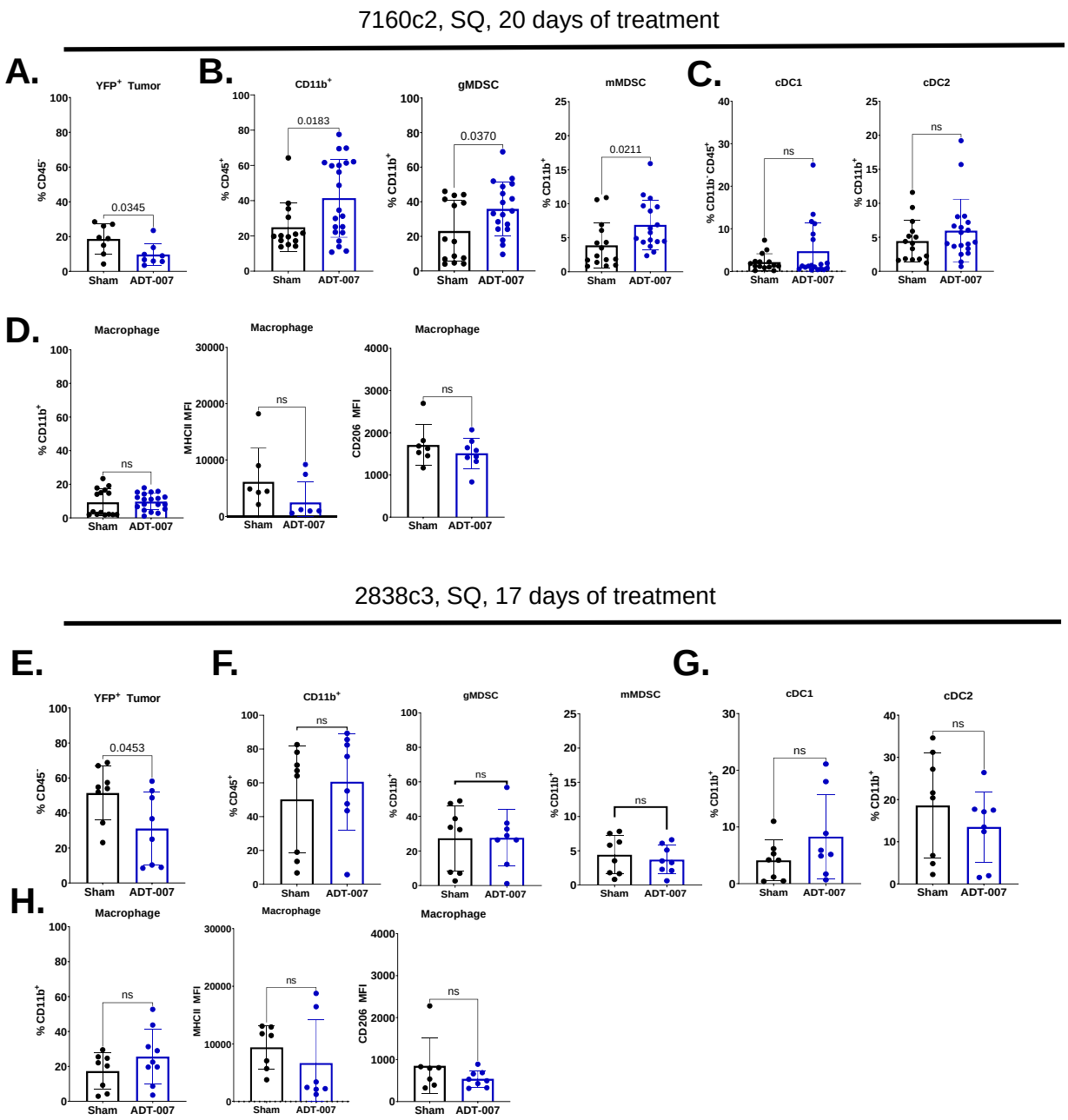


**<u>Figure 5. ADT-007 increases myeloid cell infiltrates into the 7160c2 but not 2838c3 PDA TME.</u>** (**A-D**) At 20 days post treatment the proportions of tumor and myeloid cells were evaluated by multi-parameter flow cytometry in the 7160c2 model as illustrated in Supplemental Figure 9. (**A**) The percentages of $CD45^-$ $YFP^+$ tumor cells were decreased in ADT-007 treated mice (n=8) compared to sham (n=8). Data is representative of 2 independent experiments. p values were determined by Welch's t-test. Error bars indicate SD. (**B**) The percentages of

CD45$^+$ CD11b$^+$ myeloid, CD11b$^+$ Ly6G$^+$ Ly6C$^+$ gMDSC, and CD11b$^+$ Ly6G$^-$ Ly6C$^{hi}$ mMDSC increased in ADT-007 treated (n=8) compared to sham (n=8) treated mice. Data is representative of 2 independent experiments. p values were determined by Welch's t-test. Error bars indicate SD. (**C**) The percentages of CD11b$^-$ CD11c$^{hi}$ MHCII$^{hi}$ XCR1$^+$ cDC1 and CD11b$^+$ CD11c$^{hi}$ MHCII$^{hi}$ CD172α$^+$ cDC2 subsets increased in ADT-007 (n=8) compared to sham (n=8) treated mice. Data is from two independent experiments. p values were determined by Welch's t-test, ns indicates not significant. Error bars indicate SD. (D) The percentages of CD11b$^+$ Ly6G$^-$ Ly6C$^-$ F4/80$^+$ macrophage and median fluorescent expression of MHCII and CD206 were evaluated in ADT-007 (n=8) and sham (n=7) treated mice. Data is from two independent experiments. p values were determined by Welch's t-test, ns indicates not significant. Error bars indicate SD. (**E-H**) At 17 days post treatment in the 2838c3 subcutaneous model, proportions of tumor and myeloid cells were evaluated by multi-parameter flow cytometry as indicated above. (**E**) The percentages of CD45$^-$ YFP$^+$ tumor cells were decreased in ADT-007 treated mice (n = 8) compared to sham (n=8). Data is from two independent experiments. p values were determined by Welch's t-test, ns indicates not significant. Error bars indicate SD. (**F**) The percentages of CD45$^+$ CD11b$^+$ myeloid, CD11b$^+$ Ly6G$^+$ Ly6C$^+$ gMDSC, and CD11b$^+$ Ly6G$^-$ Ly6C$^{hi}$ mMDSC were evaluated in ADT-007 treated (n=8) and sham (n=8) treated mice. Data is from two independent experiments. The p values were determined by Welch's t-test, ns indicates not significant. Error bars indicate SD. (**G**) The percentages of CD45$^+$ CD11b$^-$ CD11c$^{hi}$ MHCII$^{hi}$ XCR1$^+$ cDC1 and CD45$^+$ CD11b$^+$ CD11c$^{hi}$ MHCII$^{hi}$ CD172α$^+$ cDC2 subsets did not change in ADT-007 (n=8) and sham (n=8) treated mice. Data is from two independent experiments. p values were determined by Welch's t-test, ns indicates not significant. Error bars indicate SD. (**H**) The percentages of CD11b$^+$ Ly6G$^-$ Ly6C$^-$ F4/80$^+$ macrophage and median fluorescent expression of MHCII and CD206 were evaluated in ADT-007 (n=8) and sham (n=8) treated mice. Data is from two independent experiments. p values were determined by Welch's t-test, ns indicates not significant. Error bars indicate SD.

7160c2, SQ, 20 days of treatment

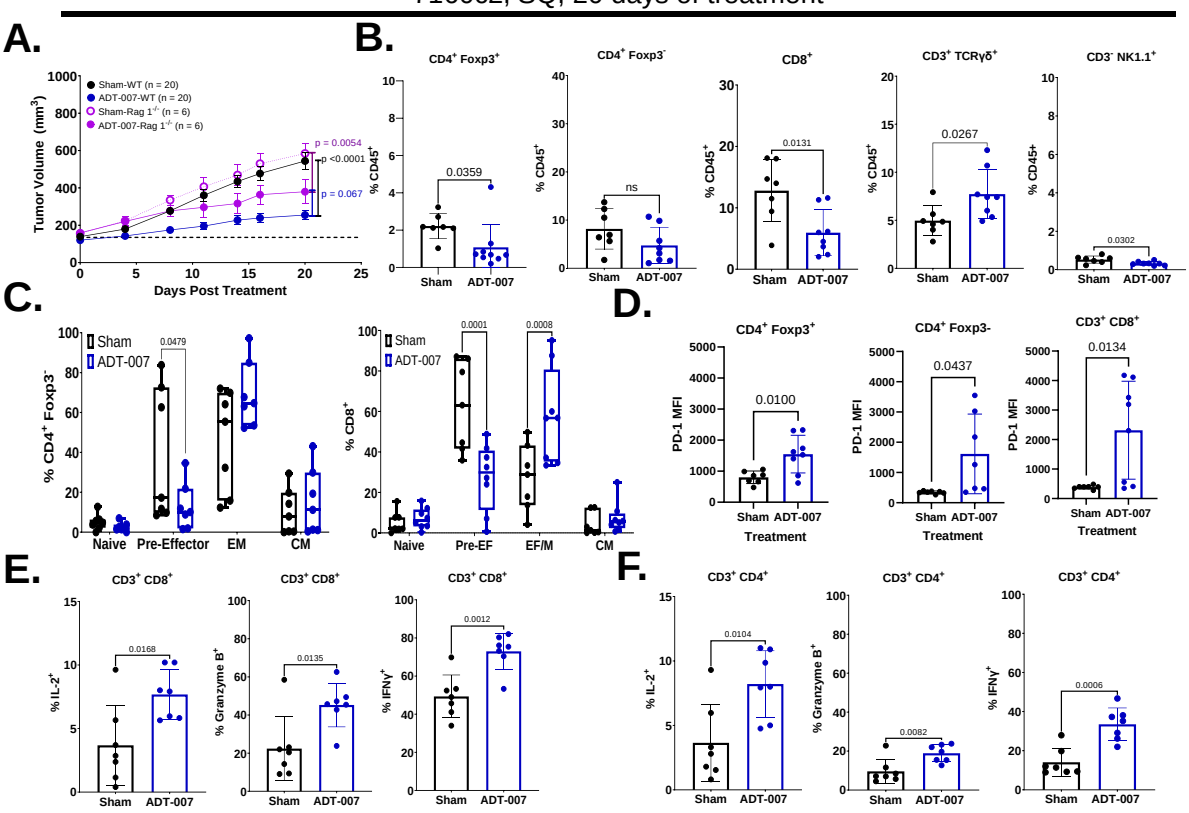


2838c3, SQ, 17 days of treatment

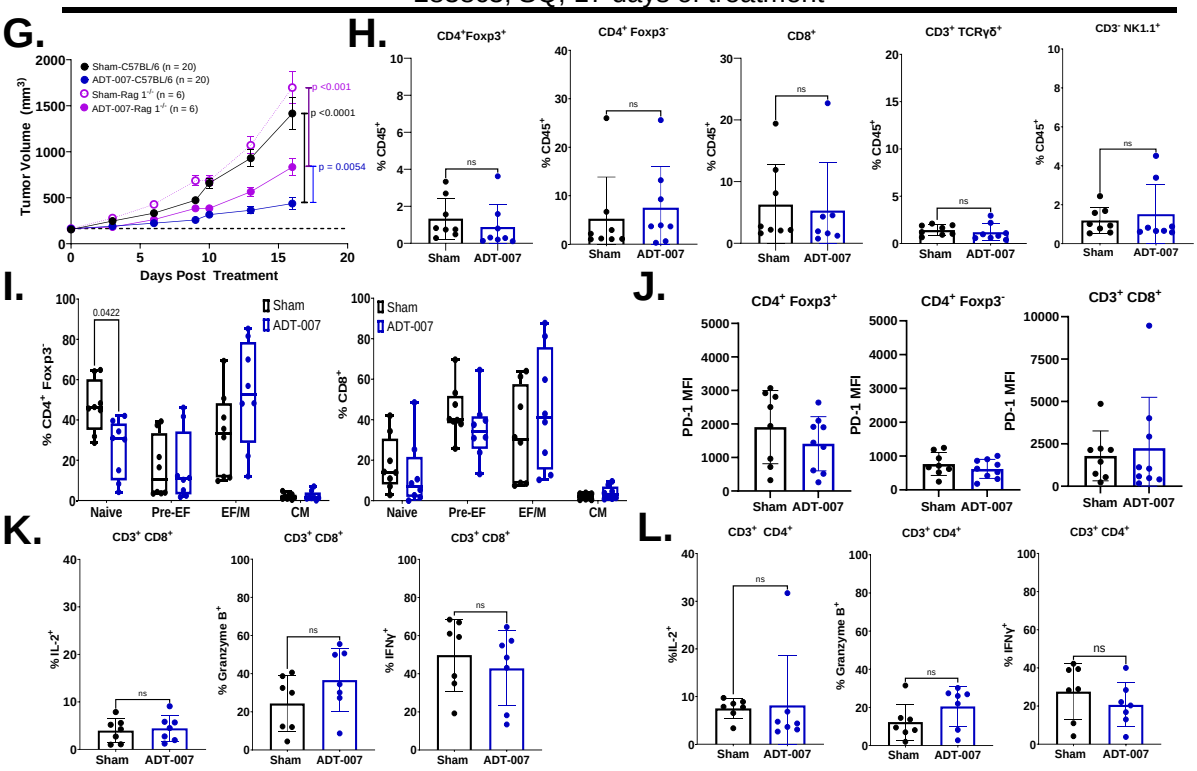


1047

**Figure 6. ADT-007 induces T cell activation and enhances cytotoxic function in PDA mouse models. (A-F)** Data is from the 7160c2 PDA model. Tumor growth in (**A**) 7160c2 PDA tumor bearing C57BL/6 WT vs. C57BL/6 Rag $1^{-/-}$ mice by peritumoral administration (5 mg/kg, BID, days 7-21, n = 6-22 mice/group, $p < 0.0001$, mean $\pm$ SE). Data is an aggregate from two separate experiments. At 20 days post treatment in 7160c2 tumor bearing mice (**B**) proportions of $CD4^+$ $Foxp3^-$, $CD4^+$ $Foxp3^+$, $CD8^+$ T cells, γδ T, and NK cells in 7160c2 PDA TME were determined by multi-parameter flow cytometry as indicated in supplemental figure 10 in ADT-007 (n=8) and sham (n=8) treated mice. Data is representative of 3 independent experiments. p values were determined by Welch's unpaired t-test, ns indicates not significant. Error bars indicate SD. (**C**) Expression of CD44 and CD62L in $CD4^+$ and $CD8^+$ T cell subsets from 7160c2 TME were evaluated by multi-parameter flow cytometry to determine percentages of naïve ($CD44^-$ $CD62L^+$), pre-effector ($CD44^-$ $CD62L^-$), effector memory ($CD44^+$ $CD62L^-$), and central memory T cells ($CD44^+$ $CD62L^+$) in ADT-007 (n=8) and sham (n=8) treated mice. Data is representative of three independent experiments. p values were determined by Welch's t-test, ns indicates not significant. Error bars indicate SD. (**D**) Expression of PD-1 in $CD4^+$ and $CD8^+$ T cell subsets from 7160c2 TME was graphed as mean fluorescent intensity. Data is representative of three independent experiments. p values were determined by Welch's t-test, ns indicates not significant. Error bars indicate SD. (**E+F**) Cytokine (IL-2, granzyme B, and IFNγ) production from (**E**) $CD4^+$ and (**F**) $CD8^+$ T cells within 7160c2 TME were evaluated after 5-hour stimulation with PMA/ionomycin in the presence of brefeldin A in ADT-007 (n=8) or sham (n=8) treated mice. Data is representative of two independent experiments. p-values were determined by Welch's unpaired t-test, ns indicates not significant. Error bars indicate SD. (**F-K**) Data is from 2838c3 PDA model. (**F**) Tumor growth in 2838c3 PDA tumor bearing C57BL/6 WT vs. C57BL/6 Rag $1^{-/-}$ mice by peritumoral administration (5 mg/kg, BID, days 7-21, n = 6-19 mice/group, $p < 0.0001$, mean $\pm$ SE). Data is an aggregate of 2 separate experiments. (**G**) proportions of $CD4^+$ $Foxp3^-$, $CD4^+$ $Foxp3^+$, $CD8^+$ T cells, γδ T and NK cells in 2838c3 TME were

determined by multi-parameter flow cytometry after 17 days of ADT-007 (n = 8) and sham (n = 8) treatment. Data is representative of 2 independent experiments. p values were determined by Welch's t-test, ns indicates not significant. Error bars indicate SD. (**H**) Expression of CD44 and CD62L in 2838c3 tumor infiltrating $CD4^+$ and $CD8^+$ T cell subsets were evaluated by multi-parameter flow cytometry to determine percentages of naïve ($CD44^-$ $CD62L^+$), pre-effector ($CD44^-$ $CD62L^-$), effector memory ($CD44^+$ $CD62L^-$), and central memory T cells ($CD44^+$ $CD62L^+$) in ADT-007 (n = 8) and sham (n = 8) treated mice. Data is representative of 2 independent experiments. p values were determined by Welch's t-test, ns indicates not significant. Error bars indicate SD. (**I**) Expression of PD-1 in $CD4^+$ and $CD8^+$ T cell subsets from 2838c3 TME was graphed as mean fluorescent intensity. Data is representative of 3 independent experiments. p values were determined by Welch's t-test, ns indicates not significant. Error bars indicate SD. (**J+K**) Cytokine (IL-2, granzyme B, and IFNγ) production from 2838c3 tumor infiltrating (**J**) $CD4^+$ and (**K**) $CD8^+$ T cells were evaluated after 5-hour stimulation with PMA/ionomycin in the presence of brefeldin A in ADT-007 (n = 8) or sham (n = 8) treated mice. Data is representative of 2 independent experiments. p-values were determined by the Student's unpaired t-test, ns indicates not significant. Error bars indicate SD.

**Supplemental figures and legends:**

**A.**

| PDAC Cell Line | KRAS Mutation | ADT-007 $IC_{50}$ (nM) |
|---|---|---|
| MIA PaCa-2 | G12C | 2.1 |
| Panc-1 | G12D | 5.8 |
| SW-1990 | G12D | 2.4 |
| CFPAC-1 | G12V | 6.3 |
| BxPC-3 | WT | 2500 |

**B.**

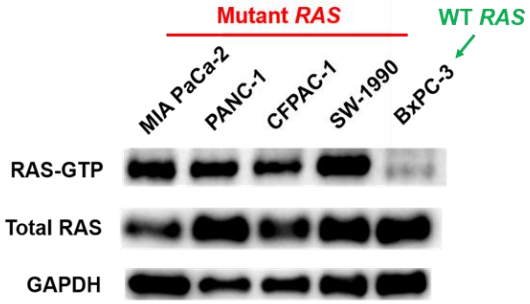


**Supplemental Figure 1. ADT-007 selectively inhibits human pancreatic cancer cell lines with mutant KRAS. (A)** Average growth $IC_{50}$ values in MIA PaCa-2, PANC-1, SW-1990, CFPAC-1, BxPC-3 were determined by Cell Titer Glo assay following 96 hours of treatment. Data is representative of at least two experiments. KRAS mutations are shown for each cell line. **(B)** Active RAS levels in PDA cell lines used for growth assays as measured by RAS-RBD pulldown assays. Data is representative of three independent experiments.

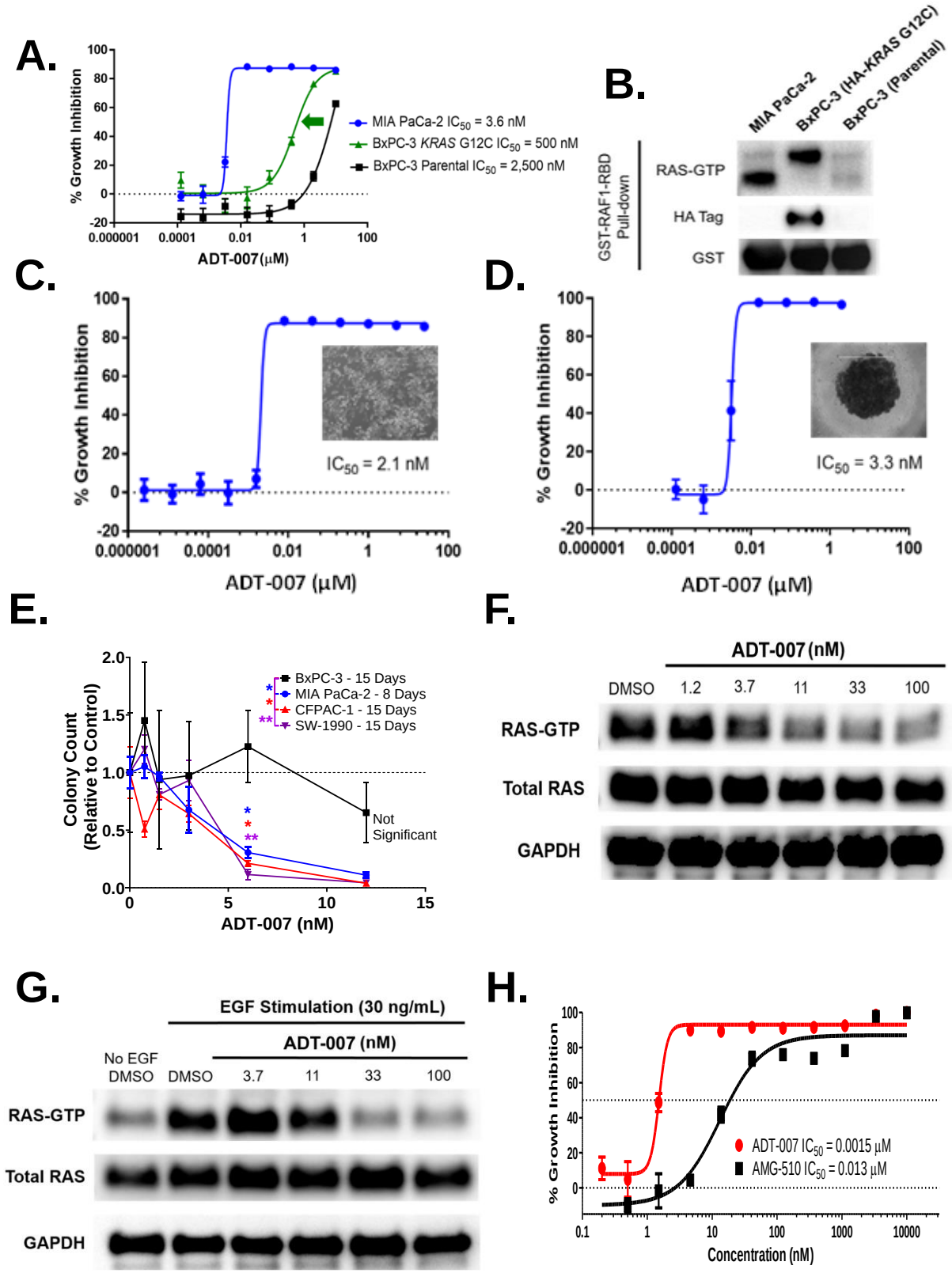
A.
% Growth Inhibition
ADT-007 (μM)
MIA PaCa-2 IC50 = 3.6 nM
BxPC-3 KRAS G12C IC50 = 500 nM
BxPC-3 Parental IC50 = 2,500 nM
B.
MIA PaCa-2
BxPC-3 (HA-KRAS G12C)
BxPC-3 (Parental)
GST-RAF1-RBD Pull-down
RAS-GTP
HA Tag
GST
C.
% Growth Inhibition
IC50 = 2.1 nM
ADT-007 (μM)
D.
% Growth Inhibition
IC50 = 3.3 nM
ADT-007 (μM)
E.
Colony Count (Relative to Control)
BxPC-3 - 15 Days
MIA PaCa-2 - 8 Days
CFPAC-1 - 15 Days
SW-1990 - 15 Days
Not Significant
ADT-007 (nM)
F.
ADT-007 (nM)
DMSO
1.2
3.7
11
33
100
RAS-GTP
Total RAS
GAPDH
G.
EGF Stimulation (30 ng/mL)
ADT-007 (nM)
No EGF DMSO
DMSO
3.7
11
33
100
RAS-GTP
Total RAS
GAPDH
H.
% Growth Inhibition
ADT-007 IC50 = 0.0015 μM
AMG-510 IC50 = 0.013 μM
Concentration (nM)

1110

**Supplemental Figure 2. Characterization of the growth inhibitory activity of ADT-007.** (**A**) Introduction of $KRAS^{G12C}$ mutation into $KRAS^{WT}$ BxPC-3 cells increases sensitivity to ADT-007. $KRAS^{G12C}$ expressed in BxPC-3 cells rendered the cells sensitive to ADT-007-mediated growth inhibition after 96 hours of treatment (Cell Titer Glo Assay). The results shown are representative of three independent experiments with samples run in triplicate. Error bars represent standard error (SEM). (**B**) Activated (GTP-RAS) was measured by RAS-RBD pull-down assays followed by WB using a pan-RAS antibody, HA-tag and GST antibody. (**C-D**) Growth inhibitory activity of ADT-007 in (**C**) spheroid or (**D**) monolayer cultures of MIA PaCa-2 cells as measured by Cell Titer Glo assay. Data is representative of three experiments; error bars represent SEM. (**E**) Inhibition of tumor cell growth in the presence of ADT-007 was evaluated in colony formation assays. The assay was terminated for each respective cell line when at least 50 distinct colonies appeared in the vehicle control group. Differences in colony counts of MIA PaCa-2, CFPAC-1, and SW-1990 at 12 nM were statistically significant from vehicle controls, while BxPC-3 exhibited no statistically significant reduction in colony count. Curves are graphed as the average of 3 replicates ± SEM. (One-way ANOVA; $*p<0.05$ vs. the vehicle (DMSO) control for each indicated cell line). Results shown are representative of at least two independent experiments. (**F**) $KRAS^{G12C}$ mutant MIA PaCa-2 PDA cells were grown under standard serum containing conditions and treated overnight with ADT-007. RAS-GTP measured by RAS-RBD pull-down assays followed by WB using a pan-RAS antibody. Data is representative of at least two independent experiments. **(G)** $KRAS^{G12C}$ mutant MIA PaCa-2 PDA cells were serum-starved, treated overnight with ADT-007, and EGF stimulated (10 mins). RAS-GTP measured by RAS-RBD pull-down assays followed by WB using a pan-RAS antibody. Data is representative of at least two independent experiments.

(**H**) Growth inhibitory activity of ADT-007 versus AMG-510 in $KRAS^{G12C}$ MIA PaCa-2 PDA cells following 72 hours of treatment as measured by Cell Titer Glo assay. Data is representative of 3 independent experiments. Error bars indicate SEM.

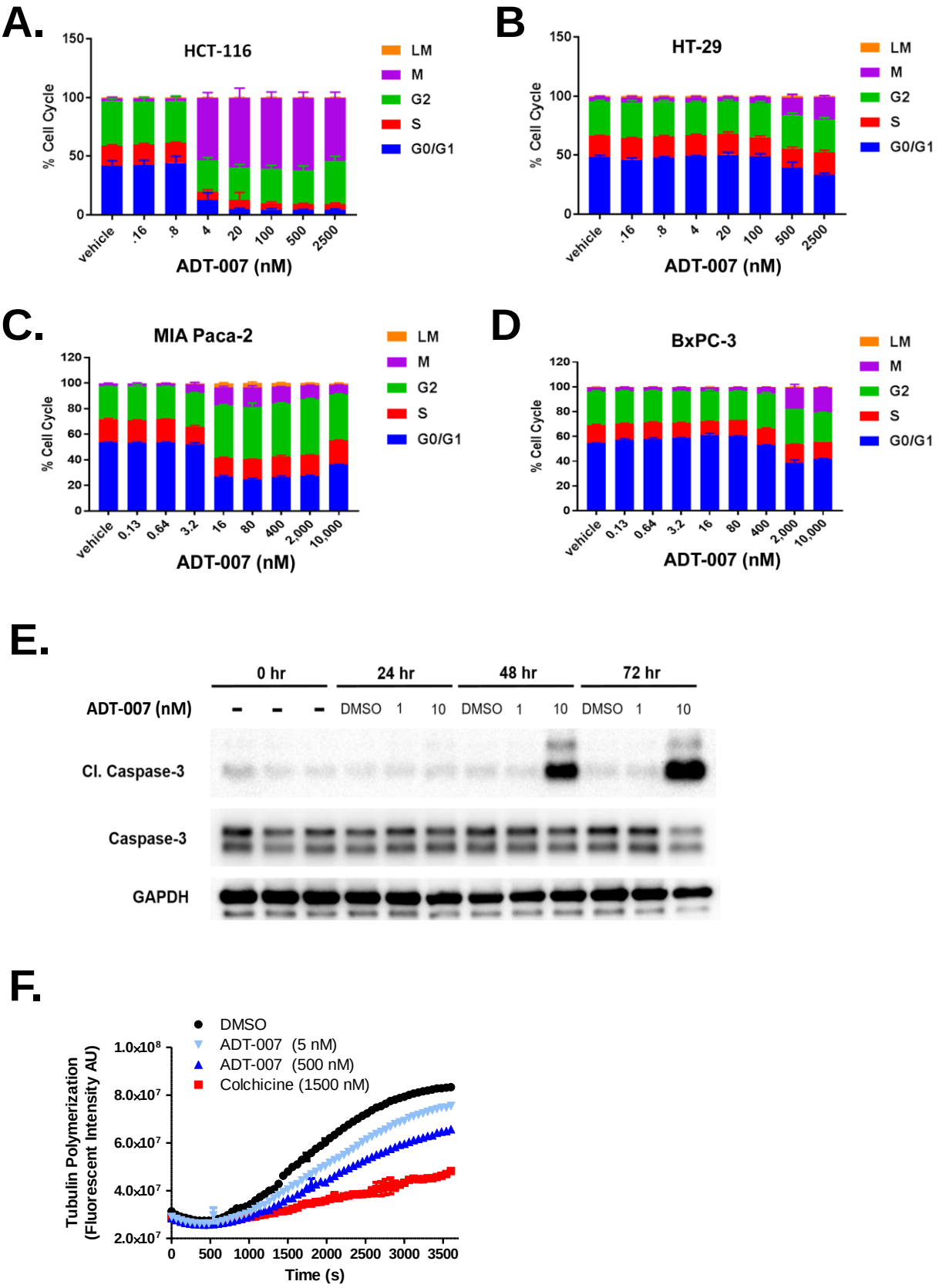
A.
HCT-116
% Cell Cycle
150
100
50
0
vehicle
.16
.8
4
20
100
500
2500
ADT-007 (nM)
LM
M
G2
S
G0/G1
B
HT-29
% Cell Cycle
150
100
50
0
vehicle
.16
.8
4
20
100
500
2500
ADT-007 (nM)
LM
M
G2
S
G0/G1
C.
MIA Paca-2
% Cell Cycle
120
100
80
60
40
20
0
vehicle
0.13
0.64
3.2
16
80
400
2,000
10,000
ADT-007 (nM)
LM
M
G2
S
G0/G1
D
BxPC-3
% Cell Cycle
120
100
80
60
40
20
0
vehicle
0.13
0.64
3.2
16
80
400
2,000
10,000
ADT-007 (nM)
LM
M
G2
S
G0/G1
E.
0 hr
24 hr
48 hr
72 hr
ADT-007 (nM)
-
-
-
DMSO
1
10
DMSO
1
10
DMSO
1
10
Cl. Caspase-3
Caspase-3
GAPDH
F.
DMSO
ADT-007 (5 nM)
ADT-007 (500 nM)
Colchicine (1500 nM)
Tubulin Polymerization
(Fluorescent Intensity AU)
1.0x10⁸
8.0x10⁷
6.0x10⁷
4.0x10⁷
2.0x10⁷
0
500
1000
1500
2000
2500
3000
3500
Time (s)

1137

**Supplemental Figure 3. ADT-007 induces cell cycle arrest at G2/M phases and induces apoptosis of human CRC and PDA cell lines *in vitro*.** (**A-D**) ADT-007 induced G2/M cell cycle arrest in (**A, C**) $KRAS^{G13D}$ HCT-116 or $KRAS^{G12C}$ MIA PaCa-2 but not (**B, D**) $KRAS^{WT}$ HT-29 or BxPC-3 cells following 24 hours of treatment. Error bars represent SEM of quadruplicate samples. (**E**) Time-dependent induction of apoptosis in $KRAS^{G12C}$ mutant MIA PaCa-2 cells by ADT-007 as measured by WB using an antibody against cleaved caspase-3. **(F)** Kinetic assay of polymerization of fluorescently labeled, purified porcine tubulin isolated from brain incubated with indicated duplicate samples of ADT-007 for 1h. Error bars represent SEM.

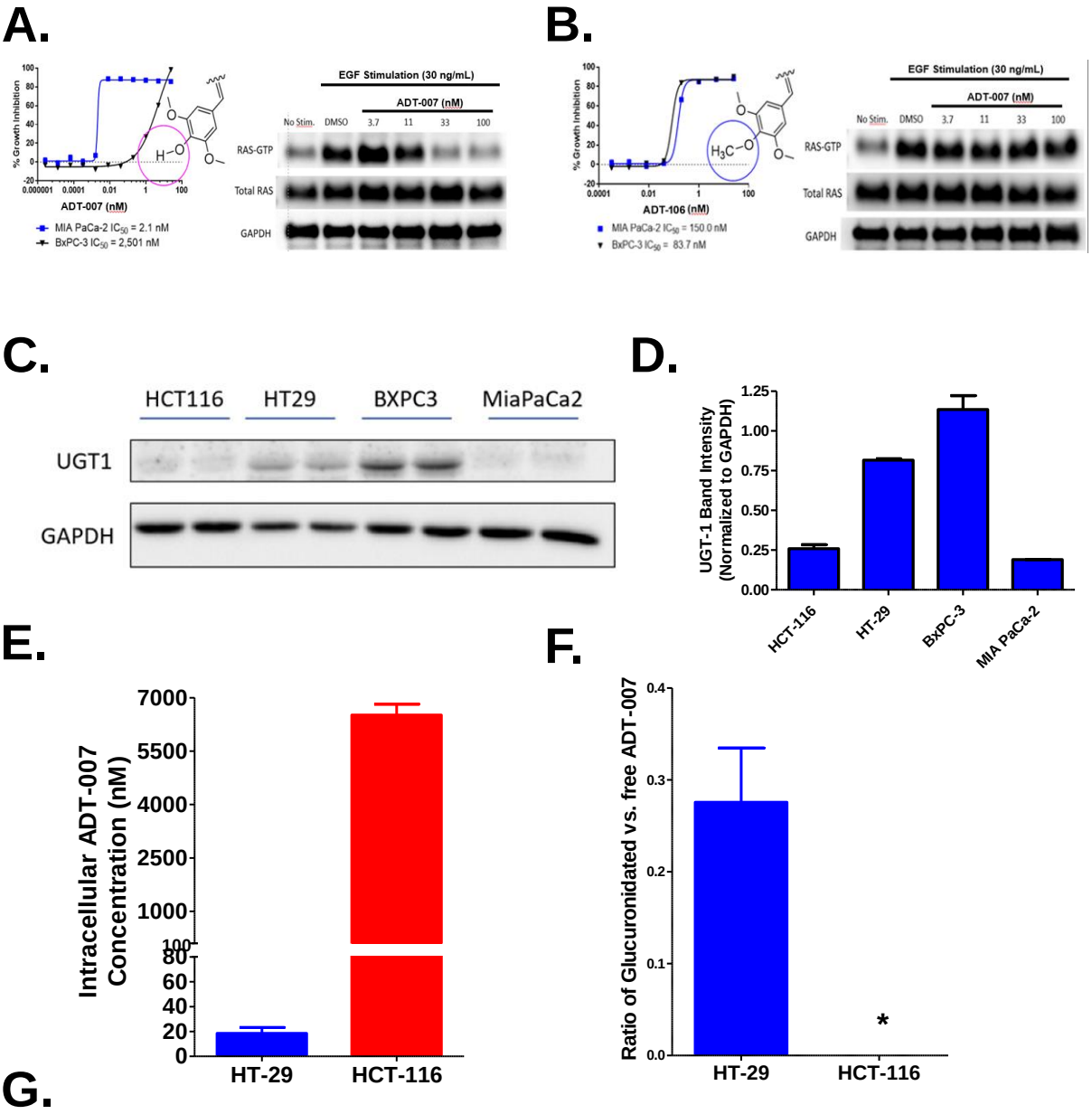


| Cell Line | Mutation Status | ADT-007 $IC_{50}$ (nM) | ADT-007 + propofol | Fold Change |
|---|---|---|---|---|
| MIA PaCa-2 | KRAS G12C | 1.8 | 1.3 | 1.4 |
| HCT-116 | KRAS G13D | 7.3 | 2.4 | 3.0 |
| BxPC-3 | WT RAS/mut BRAF | 1813 | 98.3 | 18.4 |
| HT-29 | WT RAS/mut BRAF | 3160 | 122 | 25.9 |

**Supplemental Figure 4. Phenolic moiety is critical for RAS selectivity of ADT-007-. (A)** Left panel: ADT-007 selectively inhibits growth of mutant $KRAS^{G12C}$ mutated MIA PaCa-2 PDA cells vs. $KRAS^{WT}$ BxPC-3 following 72 hours of treatment (Cell Titer Glo Assay)**.** Samples were run in

triplicate. Error bars represent standard error (SEM). Right panel: Cells were treated for 18 hours and lysates probed for activated RAS by RAS-RBD pulldown assays or WB analysis. **(B)** Left panel: ADT-106 lacking a phenolic OH moiety exhibited appreciably less potent growth inhibition following 72 hours of treatment (Cell Titer Glo Assay)**.** Samples were run in triplicate. Error bars represent standard error (SEM). Right panel: cells were treated for 18 hours and lysates probed for activated RAS by RAS-RBD pulldown assay or WB. **(C)** UGT1 enzyme expression levels in ADT-007 sensitive versus resistant cell as measured by WB. (**D**) Total GAPDH expression was used to normalize total protein loading. Differences in UGT1 protein expression were quantified in image J. **(E, F)** ADT-007 and ADT-007-glucuronide were quantified in triplicate samples of cell pellets by LC-MS/MS. Error bars represent standard error (SEM), * = $p < 0.05$. (**G**) ADT-007 resistant $RAS^{WT}$ BxPC-3 and HT-29 cells, were selectively sensitized to the compound by co-treatment with an excess of the UGT substrate, propofol (200 µM), compared with ADT-007 sensitive $KRAS^{G12C}$ MIA PaCa-2 and $KRAS^{G13D}$ mutant HCT-116 cells. Curves representative of triplicate samples in two independent experiments.

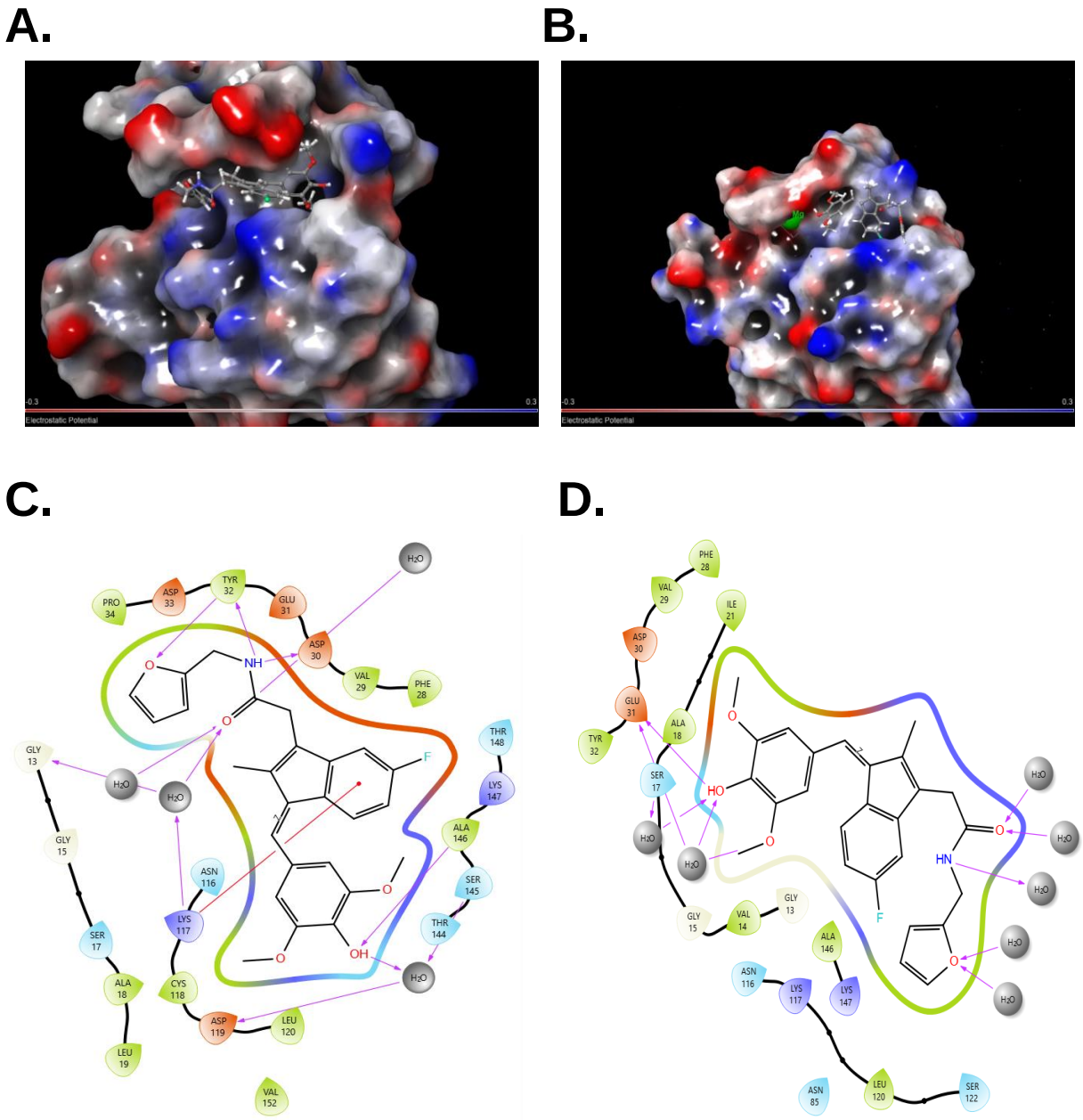


**Supplemental Figure 5**. **Molecular modeling of predicted ADT-007 binding to KRAS$^{WT}$. (A)** Docking of ADT-007 to 4OBE (KRAS$^{WT}$ Mg+2 absent). Docking Score -12.06. 4OBE is rendered as a surface representation with the electrostatic potential mapped onto the surface. ADT-007 is rendered as a ball-and-stick representation. **(B)** Docking of ADT-007 to 4OBE (KRAS$^{WT}$ Mg+2 present, green). Docking Score -11.08. 4OBE is rendered as a surface representation with the electrostatic potential mapped onto the surface. ADT-007 is rendered as a ball-and-stick

representation. **(C)** Interaction diagram of docking of ADT-007 to 4OBE (WT-KRAS Mg+2 absent). Docking Score -12.06. **(D)** Interaction diagram of docking of ADT-007 to 4OBE (WT-KRAS Mg+2 present). Docking Score -11.08.

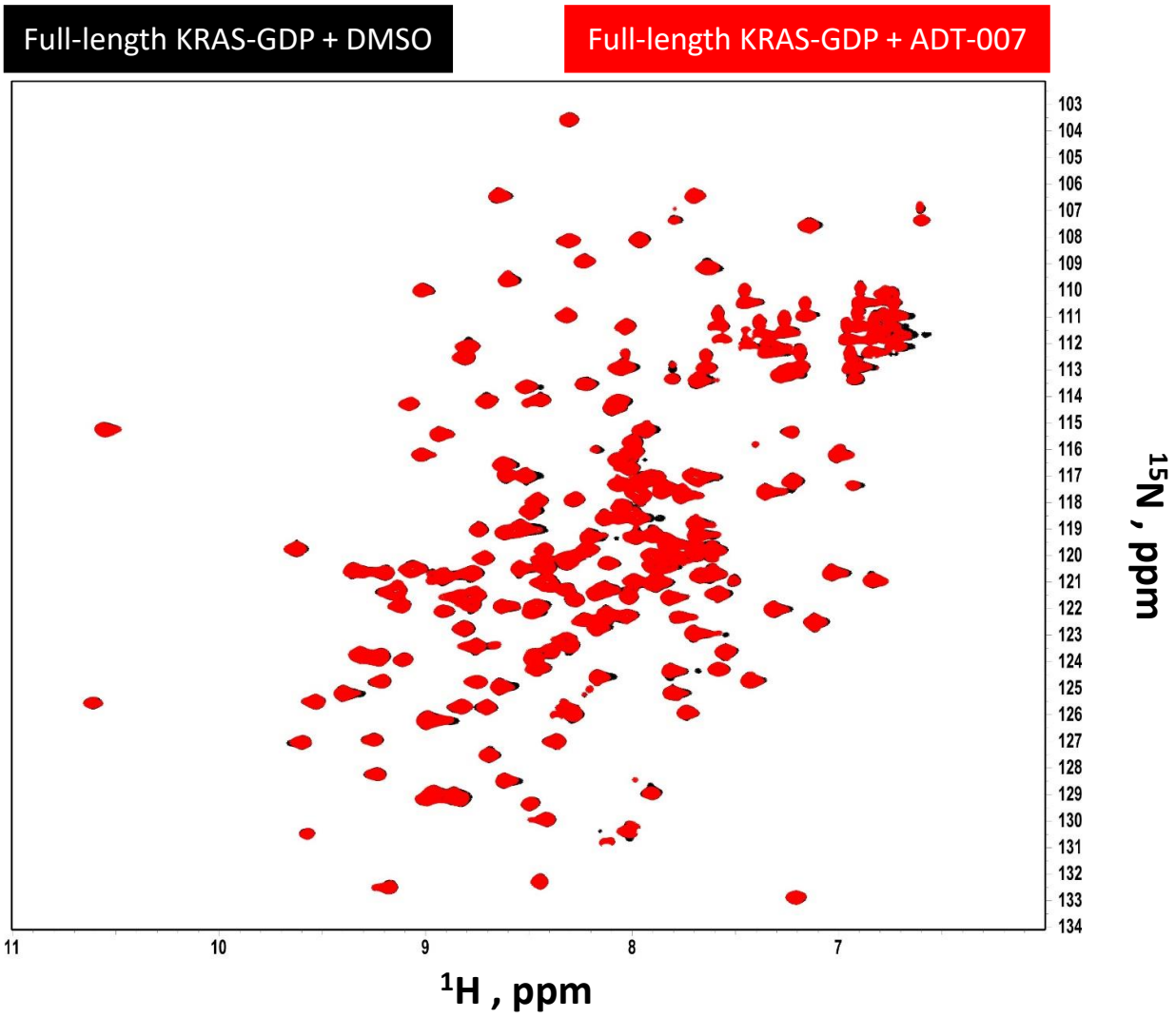


**Supplemental Figure 6. NMR analysis shows lack of ADT-007 binding to nucleotide-loaded RAS.** Overlays of $^{15}$N-HSQC spectra of 100 µM GDP-KRAS with (red) and without 125 µM ADT-007 (black) resulted in no evidence of ADT-007 binding to the inactive form of KRAS.

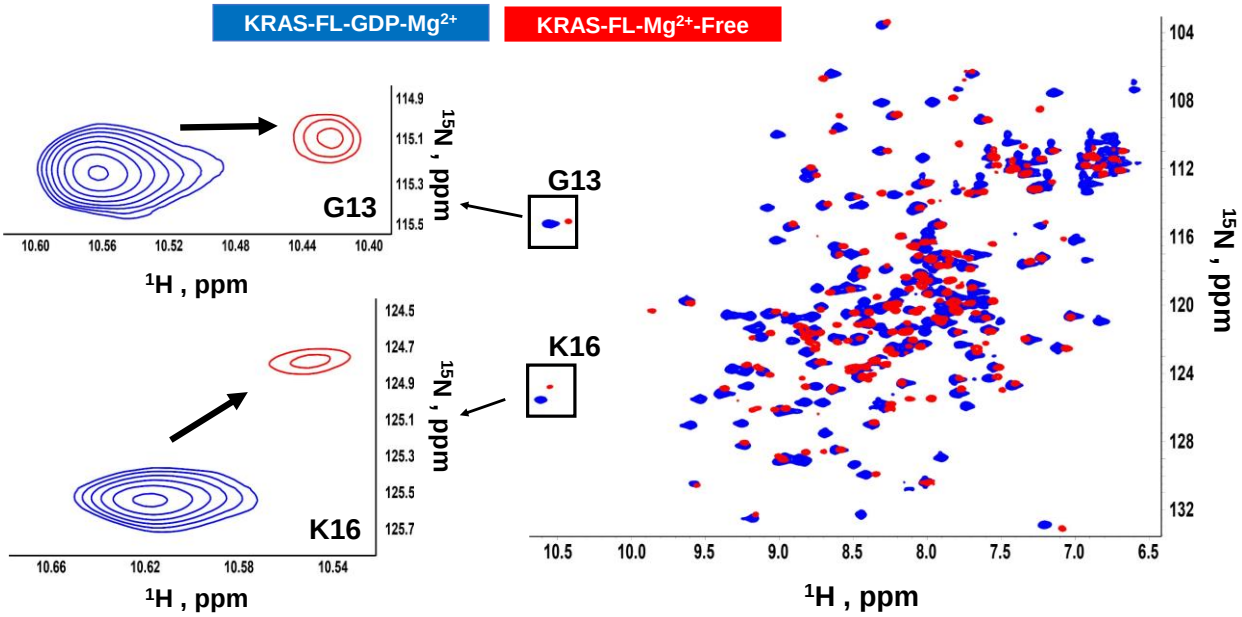


**Supplemental Figure 7. NMR analysis shows spectral differences between GDP-loaded RAS and nf-RAS.** Spectral overlays of 25 µM KRAS before (black) and after $Mg^{2+}$ chelation (blue) resulted in a structurally unique state of KRAS. Assignments for G13 and K16 due to their unique resonance frequencies are shown as a larger image to the left.

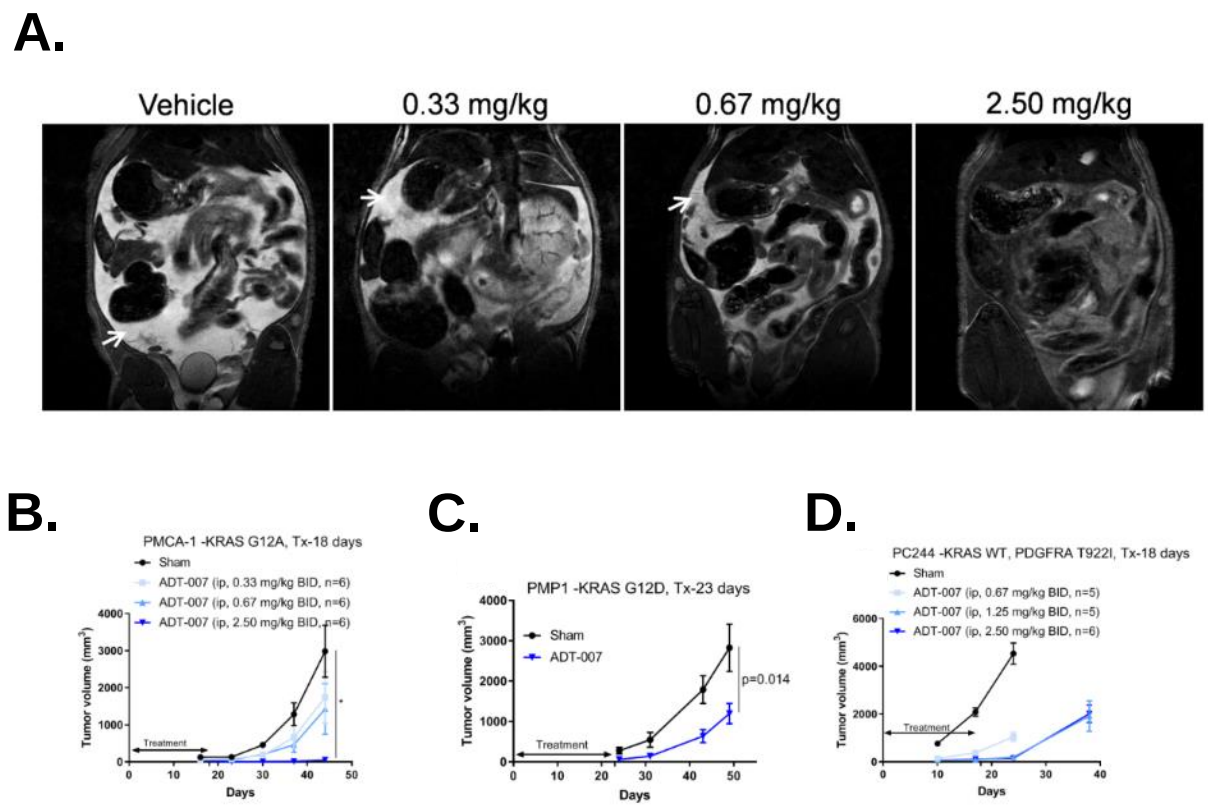


**Supplemental Figure 8. ADT-007 inhibits growth of peritoneal, mucinous CRC patient derived xenografts in a dose dependent fashion. (A)** Representative MR images taken on day 44 of mice with PMCA-1 treated with vehicle, 0.33, 0.67 or 2.50 mg/kg ADT-007 twice daily. White arrows indicate mucin. Tumor growth of **(B)** PMCA-1**, (C)** PMP-1 and **(D)** PC244. Tumor growth was monitored and quantified via MRI. Data is summarized as mean values and error bars indicate SEM and contains 5-6 mice/group**.**

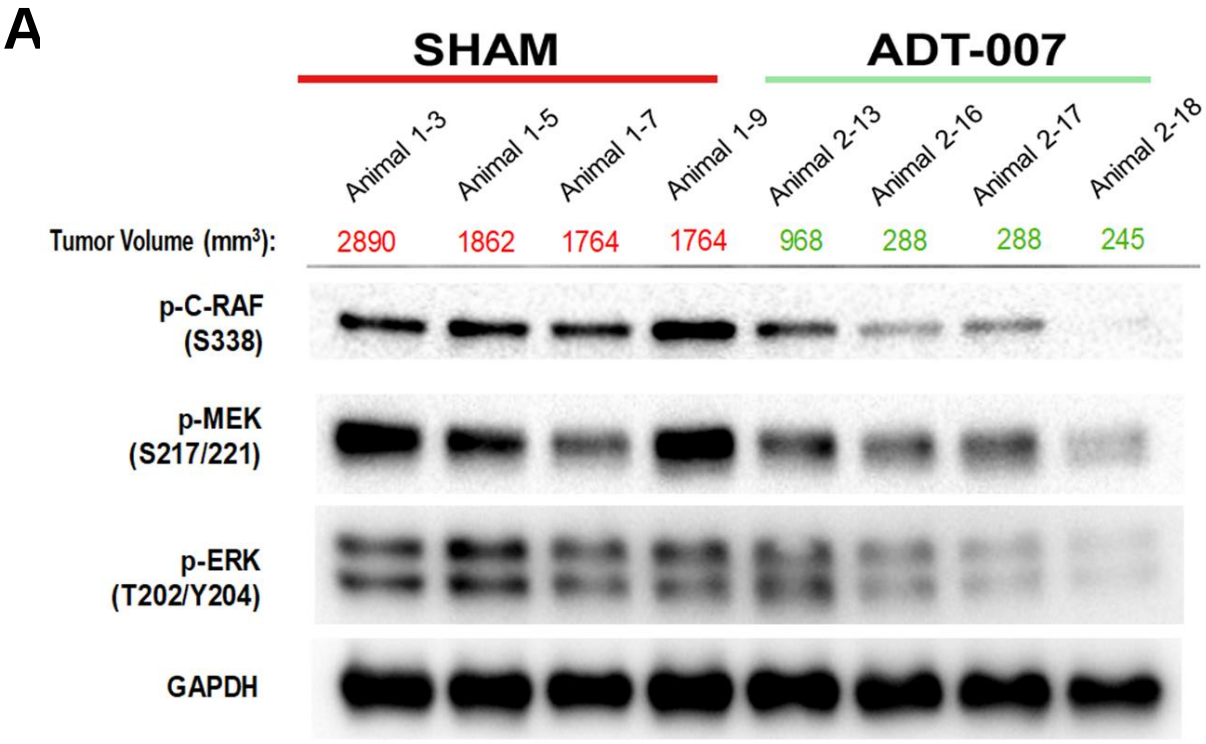
A
SHAM
ADT-007
Animal 1-3
Animal 1-5
Animal 1-7
Animal 1-9
Animal 2-13
Animal 2-16
Animal 2-17
Animal 2-18
Tumor Volume (mm³):
2890
1862
1764
1764
968
288
288
245
p-C-RAF (S338)
p-MEK (S217/221)
p-ERK (T202/Y204)
GAPDH

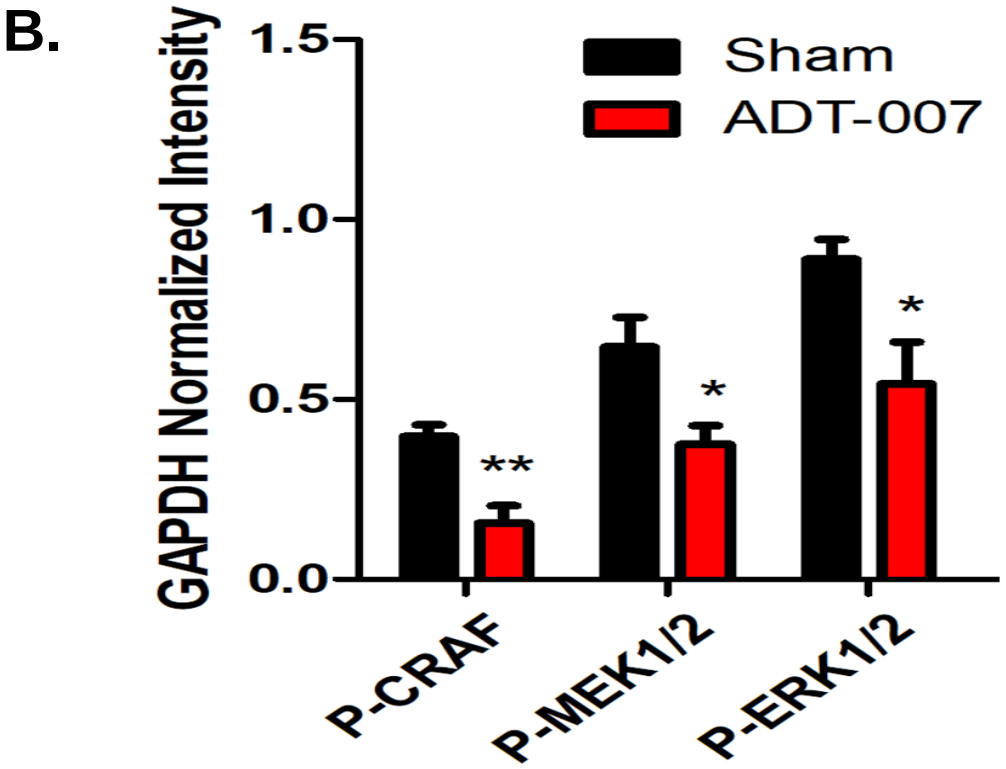
B.
GAPDH Normalized Intensity
1.5
1.0
0.5
0.0
Sham
ADT-007
**
*
*
P-CRAF
P-MEK1/2
P-ERK1/2

1194

**Supplemental Figure 9. ADT-007 inhibits RAS-MAPK signaling *in vivo* and induces T cell responses in the CT-26 CRC model. (A)** At 15 days post ADT-007 treatment in KRAS$^{G12D}$ mutant CT26 CRC model, tumor lysates were prepared to determine *in vivo* activity of ADT-007 on the RAS-MAPK pathway. ADT-007 reduces MAPK signaling (reduced p-C-RAF, p-MEK, and p-ERK) in excised tumors from mice shown in Figure 4E after the last ADT-007 injection. Tumors were collected and homogenized to evaluate phosphorylated RAF, MEK, and ERK levels by WB analysis. Each lane corresponds to a single mouse from the control or treatment (n=4) groups. GAPDH was used as a loading control. Data is representative of two independent experiments containing 4-5 mice/group. **(B)** Band density for p-cRAF, p-MEK1/2, and p-ERK1/2 were evaluated comparing sham vs. ADT-007 treated using imageJ. Statistical significance was evaluated using Welch's t-test and significance was annotated as follows: * $p < 0.05$, ** $P < 0.01$

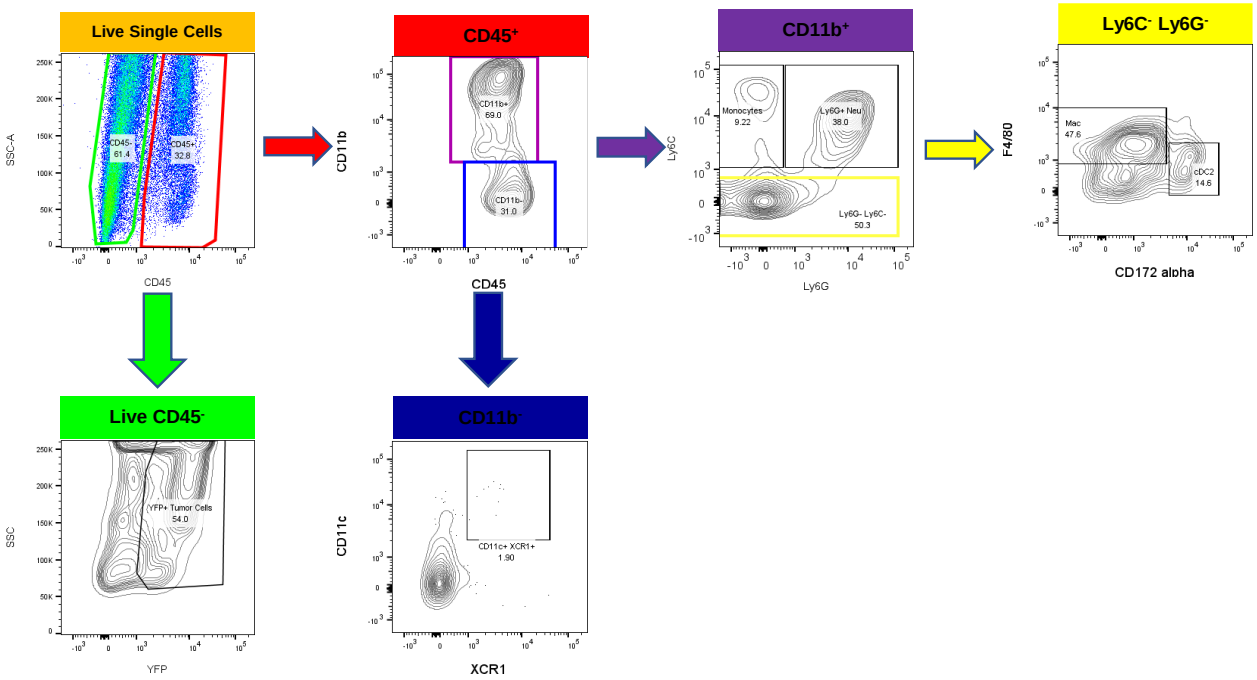


**Supplemental Figure 10. Representative gating scheme for myeloid and tumor cells.** Live-Dead Aqua negative CD45$^{+}$ and CD45$^{-}$ cells were gated upon and then myeloid cells were identified based on CD11b and CD11c expression, whereas tumor cells were identified by YFP fluorescence. The myeloid subsets were identified as follows: (i) mMDSC (CD11b$^{+}$ Ly6C$^{hi}$

Ly6G$^{-}$), gMDSC (CD11b$^{+}$ Ly6C$^{int}$ Ly6G$^{+}$), cDC2 (CD11b$^{+}$ CD11c$^{+}$ MHCII$^{+}$ F4/80$^{-}$ CD172α$^{+}$), macrophage (CD11b$^{+}$ Ly6C$^{-}$ Ly6G$^{-}$ F4/80$^{+}$), and cDC1 (**CD11b$^{-}$ gate**: CD11c$^{+}$ MHCII$^{+}$ XCR1$^{+}$). Expression (MFI) of MHCII and CD206 were evaluated in macrophages to determine activation and polarization status of specific subsets.

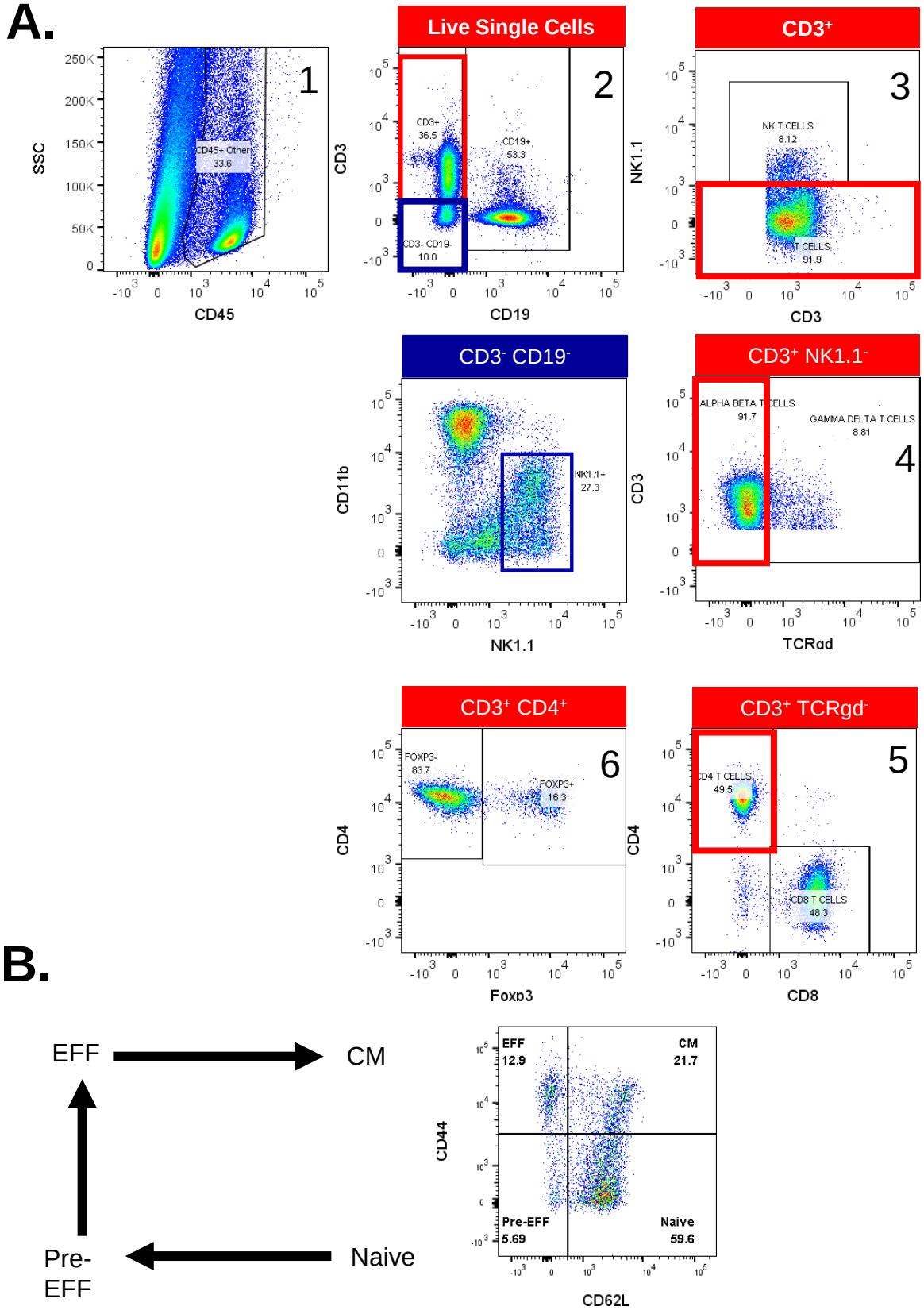
A.
Live Single Cells
CD3+
CD3- CD19-
CD3+ NK1.1-
CD3+ CD4+
CD3+ TCRgd-
1
2
3
4
5
6
SSC
CD45
CD45+ Other
33.6
CD3
CD19
CD3+
36.5
CD19+
53.3
CD3- CD19-
10.0
NK1.1
NK T CELLS
8.12
T CELLS
91.9
CD11b
NK1.1
NK1.1+
27.3
ALPHA BETA T CELLS
91.7
GAMMA DELTA T CELLS
8.81
TCRgd
FOXP3-
83.7
FOXP3+
16.3
CD4
Foxp3
CD4 T CELLS
49.5
CD8 T CELLS
48.3
CD8
B.
EFF
CM
Pre-EFF
Naive
EFF
12.9
CM
21.7
Pre-EFF
5.69
Naive
59.6
CD44
CD62L

1215

**Supplemental Figure 11. Representative gating scheme for T and NK cells.** Live-Dead Aqua negative CD45$^+$ cells were gated upon to identify NK and T cells as follows: NK (NK1.1$^+$ CD3$^-$), NKT (NK1.1$^+$ CD3$^+$), γδ T (CD3$^+$ TCRγδ$^+$), helper T (CD3$^+$ CD4$^+$) and cytotoxic T (CD3$^+$ CD8$^+$) T cells. Foxp3 expression within the CD4$^+$ T cell subset was used to identify Foxp3$^+$ regulatory T cells. Expression of PD-1, CD44, and CD62L were used to further identify activation status.

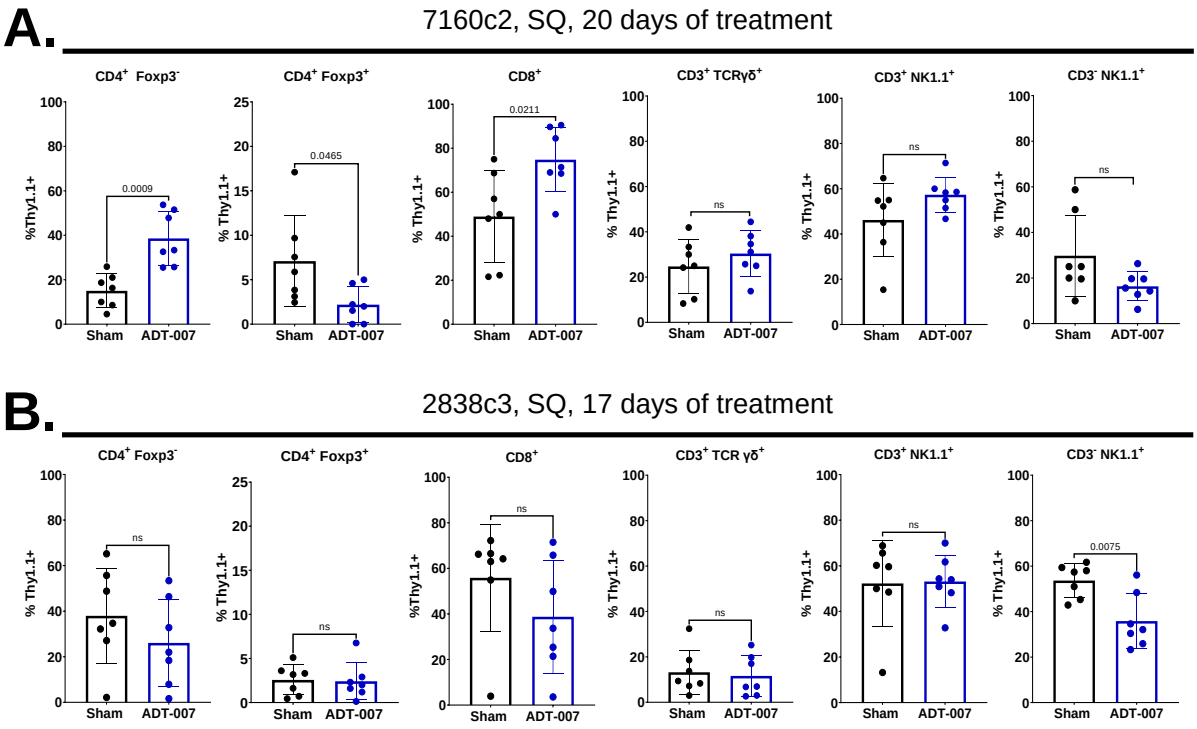


**Supplemental Figure 12. ADT-007 treatment increases IFNγ production by CD4$^+$ and CD8$^+$ T cells in the 7160c2 TiME.** (**A+B**) Production of IFNγ was evaluated in vivo by flow cytometry using Thy1.1-IFNγ reporter mice implanted with (**A**)7160c2 or (**B**) 2838c3 tumor cell lines. As in Figure 4, mice were treated with peritumoral injections of ADT-007 (5 mg/kg, BID, n = 7 mice/group) or sham for 17 days. P values were evaluated using Student's unpaired t-test. Error bars indicate SD. Data is from a single experiment.

| Type | Tissue Origin | Cell Line | Mutation Status | $IC_{50}$ (nM) | UGT1A1 mRNA | UGT1A6 mRNA | UGT1A10 mRNA | UGT2A1 mRNA | UGT2B10 mRNA | UGT2B15 mRNA | UGT2B7 mRNA |
|---|---|---|---|---|---|---|---|---|---|---|---|
| Mutant RAS, sensitive | Pancreatic | MIA PaCa-2 | KRAS G12C | 2.1 | 0 | 0.287 | 0.263 | 0 | 0 | 0 | 0.057 |
| | Pancreatic | PANC-1 | KRAS G12D | 2.4 | 0 | 0.057 | 0.043 | 0 | 0 | 0.014 | 0.029 |
| | Pancreatic | SW-1990 | KRAS G12D | 6.3 | 0 | 0 | 0.138 | 0 | 0 | 0 | 0.057 |
| | Lung | A549 | KRAS G12S | 6.8 | 0.669 | 0.791 | 0.070 | 0 | 0.014 | 0.070 | 0.202 |
| | Pancreatic | CFPAC-1 | KRAS G12V | 5.8 | 1.05 | 1.69 | 2.63 | 0 | 0 | 0.098 | 0.151 |
| | Colon | SW480 | KRAS G12V | 6.5 | 1.57 | 3.17 | 0.58 | 0 | 0 | 0 | 0.000 |
| | Breast | MDA-MB-231 | KRAS G13D | 3.6 | 0.214 | 0.807 | 0.043 | 0 | 0 | 0 | 0.043 |
| | Colon | HCT-116 | KRAS G13D | 4.7 | 0.029 | 0.189 | 0 | 0 | 0 | 0 | 0.000 |
| | Ovarian | OVCAR-8 | KRAS P121H | 5.8 | 0 | 0.214 | 0.057 | 0 | 0 | 0 | 0.000 |
| | Breast | Hs 578T | HRAS G12D | 3.9 | 0.043 | 0.163 | 0.098 | 0 | 0 | 0 | 0.098 |
| | Skin | SK-MEL-2 | NRAS Q61K | 2.1 | 0 | 0 | 0 | 0 | 0 | 0.084 | 3.531 |
| | Lung | NCI-H1299 | NRAS Q61K | 2.4 | 0 | 0.043 | 0 | 0 | 0 | 0 | 0.000 |
| WT RAS, resistant | Normal Lung | NHAEC | WT RAS | 19100 | * | * | * | * | * | * | * |
| | Normal Colon | NCM460 | WT RAS | > 25,000 | * | * | * | * | * | * | * |
| Downstream mutation (WT RAS) resistant | Ovarian | OV-90 | WT RAS/mut BRAF | 350 | 5.00 | 6.92 | 4.57 | 0.070 | 0.057 | 0.632 | 3.223 |
| | Colon | HT-29 | WT RAS/mut BRAF | 512 | 3.55 | 5.53 | 6.97 | 0 | 0.214 | 0.660 | 0.791 |
| | Skin | SK-MEL-28 | WT RAS/mut BRAF | > 25,000 | 0.00 | 0.20 | 0.14 | 0 | 0 | 0 | 3.530 |
| | Pancreatic | BxPC-3 | WT RAS/mut BRAF | 2500 | 2.11 | 6.41 | 7.75 | 0.057 | 0 | 0 | 0.433 |
| Upstream RAS activation sensitive | Lung | NCI-H1975 | WT RAS/mut EGFR | 3.9 | * | * | * | * | * | * | * |
| | Skin (mouse) | B16 | WT RAS/mut PDGFR | 5.8 | * | * | * | * | * | * | * |
| | Brain | U-87 MG | WT RAS/mut NF1 | 1.6 | 0 | 0.287 | 0 | 0 | 0 | 0 | 0.299 |
| | Ovarian | SK-OV-3 | WT RAS/mut NF1 | 6.7 | 2.89 | 7.66 | 0.202 | 0 | 0 | 0 | 4.850 |

**Supplemental Table 1. Sensitivity of tumor cells to ADT-007 is associated with high activated RAS levels and low levels of UGT superfamily enzymes.** Growth inhibitory ($IC_{50}$) values were determined by ATP content using the Promega Cell Titer Glo assay following 72-96 hours of treatment. TPM normalized expression of the most significant differentially expressed UGT enzymes were obtained from data published in the Cancer Cell Line Encyclopedia accessed via the DepMap Portal hosted by the Broad Institute.

**Supplemental Table 2. List of antibodies used for Western blot Assays.**

| Antibody | Supplier | Clone | Dilution | Reactivity | Cat # |
|---|---|---|---|---|---|
| Total RAS | ThermoFisher | Ras10 | 1-1000 | Mouse/Human | MA1-012 |
| KRAS | Santa Cruz | F234 | 1-500 | Mouse/Rat/Human | SC-30 |
| HRAS | Santa Cruz | 259 | 1-500 | Mouse/Rat/Human | SC-35 |
| NRAS | Santa Cruz | F155 | 1-250 | Mouse/Rat/Human | SC-31 |
| Total RAF | Cell Signaling | Polyclonal | 1-1000 | Human/ Mouse/ Rat | 9422 |
| p-C-RAF (S338) | Cell Signaling | 56A6 | 1-1000 | Mouse/Human/Rat | 9427 |
| Total MEK1/2 | Cell Signaling | Polyclonal | 1-1000 | Mouse/Human/Rat | 9122 |
| p-MEK1/2 (S217/221) | Cell Signaling | 41G9 | 1-1000 | Mouse/Human | 3958S |
| Total ERK1/2 | Cell Signaling | 137F5 | 1-1000 | Mouse/Human | 4695S |
| p-ERK1/2 (T202/Y204) | Cell Signaling | D13.14.4E | 1-2000 | Mouse/Human | 4370S |
| Total AKT | Cell Signaling | C67E7 | 1-1000 | Mouse/Human | 4691S |
| p-AKT (Ser473) | Cell Signaling | D9E | 1-1000 | Mouse/Human | 4060S |
| p-AKT () | Cell Signaling | D25E6 | 1-1000 | Mouse/Human | 13038S |
| GAPDH | Cell Signaling | D16H11 | 1-1000 | Mouse/Human | 5174S |

1253 **Supplemental Table 3. List of antibodies used for flow cytometry.**

| Antibody | Supplier | Clone | Dilution | Cat# |
|---|---|---|---|---|
| PD-1 FITC | BioLegend | 29F.1A12 | 1-200 | 135214 |
| CD206 FITC | BioLegend | C068C2 | 1-200 | 141703 |
| CD107α | BioLegend | ID4B | 1-1000 | 121607 |
| TIM-3 PE | BioLegend | B8.2C12 | 1-200 | 134003 |
| F4/80 PE | BioLegend | BM8 | 1-800 | 123110 |
| IL-17F PE | BioLegend | 9D3.1C8 | 1-800 | 517008 |
| Thy1.1 PE | BD | OX-7 | 1-200 | 551401 |
| CD19 PE Cy7 | BioLegend | ID3 | 1-800 | 152418 |
| Granzyme B PE Cy7 | BioLegend | GB11 | 5 uL/$10^6$ cells | 372214 |
| Ly6C PE Cy7 | BioLegend | HK1.4 | 1-3300 | 128017 |
| CD11b PE Dazzle | BioLegend | M1/70 | 1-3300 | 101255 |
| IFNγ PE Dazzle | BioLegend | XMG1.2 | 1-1000 | 505846 |
| CD45 PerCP | BioLegend | 30-F11 | 1-800 | 103130 |
| Foxp3 APC | Invitrogen | FJK-16s | 1-200 | 17-5773-82 |
| CD11c APC | BioLegend | N418 | 1-400 | 117309 |
| TNFα APC | BioLegend | MP6-XT22 | 1-1000 | 506308 |
| CTLA-4 APC R700 | BD | UC10-4F10-11 | 1-400 | 565778 |
| CD172α Alexa Flour 700 | BioLegend | P84 | 1-1000 | 144022 |
| CD62L APC Cy7 | BioLegend | MEL-14 | 1-800 | 104428 |
| CD86 APC Cy7 | BioLegend | GL1 | 1-200 | 105045 |
| IL-2 APC 750 | BioLegend | JES6-5H4 | 1-1000 | 503832 |
| CD3 BV421 | BioLegend | 145-2C11 | 1-800 | 100341 |
| XCR1 BV421 | BioLegend | ZET | 1-1000 | 148216 |
| Live/Dead Aqua | Invitrogen | n/a | 1-500 | L34966 |
| Ly6G BV570 | BioLegend | 1A8 | 5 uL/$10^6$ cells | 127629 |
| TCR γδ BV 605 | BioLegend | GL3 | 1-800 | 118219 |

| | | | | |
|---|---|---|---|---|
| PD-L1 BV 605 | BioLegend | MIH5 | 1-400 | 153606 |
| CD4 BV 650 | BioLegend | GK1.5 | 1-800 | 100469 |
| MHCII BV 650 | BioLegend | M5/114/15.2 | 1-800 | 107641 |
| NK1.1 BV 711 | BioLegend | PK136 | 1-400 | 108475 |
| CD103 BV 711 | BioLegend | 2E7 | 1-800 | 121435 |
| CD8 BV 785 | BioLegend | 53-6.7 | 1-800 | 100750 |
| CCR7 BV785 | BioLegend | 4B12 | 1-250 | 120217 |
| CD44 BUV 737 | BD | IM7 | 1-800 | 612799 |
| CD69 BUV 395 | BD | H1.2F3 | 1-400 | 569367 |
| B220 BUV 395 | BD | RA3.6B2 | 1-400 | 563793 |
| Fc Block (CD16/CD32) | BioLegend | 93 | 1-500 | 101320 |

**Supplemental Methods**

High content image-based cell cycle analysis 5,000 cells were seeded per well in Perkin Elmer ViewPlate™ microplates (Perkin Elmer, CT, USA), then incubated overnight at 37 °C. The following day, five-fold dilutions of ADT-007 or DMSO vehicle in dosing medium were added in equal volume (100 µL), to each well on the assay plate and incubated with the compounds for a further 24h. At the end of the treatment period, 150 µL per well of neutral buffered formalin fixative (10% paraformaldehyde) was rapidly added to each plate and incubated at room temperature for 20 min. Fixative was removed by washing with PBS (PBS). Plasma membranes were permeabilized by incubation with 0.3% Triton X-100 and 5% FBS in PBS for 1 h. TBS with 1 µg/mL DAPI was added to quantitate double stranded DNA within each cell nucleus. DNA content in each cell was determined by total DAPI stain intensity and assigned to the appropriate category (G0/G1, S, G2, M) using the MetaXpress cell cycle analysis program. Results from each treatment were reported as average cell number in each of nine fields, as

well as the percentage of cells within each phase of the cell cycle. Each of these parameters was analyzed using GraphPad Prism, and, where appropriate, $IC_{50}$ values have been reported.

Spheroid Cell Culture: Cells were seeded at a density of 500 cells per well in 100 µL of media in a 96-well U-bottom, nonbinding spheroid microplate (Corning). After a 4-day incubation at 37°C in a humidified incubator with 5% carbon dioxide to allow for spheroid formation, spheroids were dosed with 100 µL of compound solution at two times the desired final concentration. Average diameters of the spheroids were measured three times a week using a Celigo Imaging Cytometer (Nexcelom Bioscience). After the desired treatment duration had elapsed, 100 µL of Cell Titer-Glo assay reagent (Promega) was added to each well. The plate was incubated for 1 hour at 37°C and luminescent readings were collected according to the manufacturer's assay protocol in a Bio-Tek Synergy H4 microplate reader. Curves of tumor diameter and growth inhibition were generated using GraphPad Prism.

Colony formation assays: Suspensions of 500 cells/well (6-well plate) were incubated for 24 hours at 37°, and then dosed 24 hours later with either increasing concentrations of ADT-007 (0.5. 5, 20, 30, 40, 50, 70 nM), AMG-510 (0.5. 5, 20, 30, 40, 50, 70 nM), or DMSO and then incubated for period of 10-14 days. Endpoints were determined when 50 distinct colonies in the vehicle control wells were reached. At endpoint, wells were washed in PBS, then stained for 1 hour at RT in 2 mL of crystal violet solution in 1% formalin and 1% methanol. Plates were imaged using a ChemiDoc Imaging System (Bio-Rad, Hercules, CA), and colonies were counted using a custom macro in Nikon Elements Research developed by Dr. Joel Andrews (University of South Alabama).

Fluorescent tubulin polymerization assay: A fluorescent tubulin polymerization assay kit from Cytoskeleton, Inc. (Catalog #BK011P) was used according to the supplied protocol to determine effects of experimental compounds on tubulin polymerization. Briefly, control and test compounds were added to duplicate samples assay mix (100 ng porcine tubulin, 1 mM GTP,

25% glycerol, 2x assay buffer containing: 80 mM Piperazine-N,N'-bis[2-ethanesulfonic acid] sequisodium salt; 2.0 mM Magnesium chloride; 0.5 mM Ethylene glycol-bis(b-amino-ethyl ether) N,N,N',N'-tetra-acetic acid, pH 6.9, 10 μM fluorescent reporter( 4', 6-Diamidino-2-phenylindole). The plate was immediately transferred to a Molecular Devices Spectramax Paradigm fluorescence plate reader equilibrated to 37°C. Fluorescence (360ex/450em) was read each 1 min for 60 min at 37°C.

Histology: Tissues were fixed overnight in 10% neutral buffered formalin. Tissues were sectioned at 5 μm. Hematoxylin & Eosin and Masson's Trichrome stains were performed according to protocols established by the Comparative Pathology Lab (UAB, ARP).

Molecular Modeling: WT-KRAS (PDB entry 4OBE) was used for all modeling studies. The protein was prepared using the Protein Preparation workflow within Schrodinger 2022-3. For the $Mg^{2+}$ free form, $Mg^{2+}$ was deleted, and the resulting structure was then submitted to the work flow. Initial docking studies with ADT-007 were performed with GDP removed from KRAS using GLIDE. The highest scoring docking pose was submitted to molecular dynamics using DESMOND for 100 nsec, and the resulting trajectory file was analyzed by molecular clustering with 12 clusters resulting from each dynamics run. The highest scoring pose was then determined using GLIDE and this pose was then optimized using induced-fit docking.